NASA TECHNICAL NOTE

NASA TN D-4177

NASA TN D-4177

HEAT TRANSFER IN 30° AND 60° HALF-ANGLE OF CONVERGENCE NOZZLES WITH VARIOUS DIAMETER UNCOOLED PIPE INLETS

by Donald R. Boldman, Harvey E. Neumann, and James F. Schmidt

Lewis Research Center

Cleveland, Ohio

NATIONAL AERONAUTICS AND SPACE ADMINISTRATION • WASHINGTON, D. C. • SEPTEMBER 1967

NASA TN D-4177

HEAT TRANSFER IN 30° AND 60° HALF-ANGLE OF CONVERGENCE NOZZLES WITH VARIOUS DIAMETER UNCOOLED PIPE INLETS

By Donald R. Boldman, Harvey E. Neumann, and James F. Schmidt

Lewis Research Center
Cleveland, Ohio

NATIONAL AERONAUTICS AND SPACE ADMINISTRATION

For sale by the Clearinghouse for Federal Scientific and Technical Information
Springfield, Virginia 22151 – CFSTI price $3.00

HEAT TRANSFER IN 30° AND 60° HALF-ANGLE OF CONVERGENCE NOZZLES WITH VARIOUS DIAMETER UNCOOLED PIPE INLETS

by Donald R. Boldman, Harvey E. Neumann, and James F. Schmidt

Lewis Research Center

SUMMARY

An experimental investigation was conducted in a heated-air facility in order to determine the effects of a variation in uncooled pipe-inlet diameter and the associated contraction area ratio on the heat-transfer distributions in 30° and 60° half-angle of convergence nozzles having the same throat diameter and curvature. Tests were conducted at a nominal stagnation temperature of 970° R (539° K) and nominal stagnation pressures of 160 and 300 pounds per square inch (110 and 207 N/cm^2) absolute. Experimental heat-transfer coefficients were compared to values predicted by two interrelated boundary-layer calculation techniques and a pipe-flow (Nusselt number) type of correlation.

Pronounced increases in the experimental nozzle peak heat-transfer coefficients accompanied a reduction in contraction area ratio, other conditions remaining fixed. For the same contraction area ratio and stagnation conditions, a pronounced increase in peak heat-transfer coefficient was coincident with an increase in nozzle convergence angle.

All the prediction techniques failed to yield consistent agreement with the experimental peak heat-transfer coefficients; that is, in some cases all methods underestimated the peak values of heat-transfer coefficient, but in other cases an overprediction was evident. The overpredicted heat transfer was usually characteristic of the configurations having the largest contraction area ratio ($\approx$19).

INTRODUCTION

The design of regeneratively cooled nozzles for high performance rocket systems requires a comprehensive knowledge of the gas-side convective heat transfer. Engineering techniques for predicting the heat transfer often consist of using correlations which have been tailored to the experimental heat-transfer distributions corresponding to a certain class of nozzle geometries and flow environments (ref. 1). These correlations,

which are usually premised on flat-plate, zero pressure-gradient heat transfer, consider primarily the mass-flux variation through the nozzle. The effects of flow acceleration and turning are completely neglected. Hence, it is not surprising that a simple correlation equation failed to predict the heat transfer in a hydrogen-oxygen rocket (ref. 2) and heated air nozzles (refs. 3 and 4).

In reference 5, a Nusselt number correlation was employed in the prediction of heat transfer to 30° and 60° half-angle of convergence nozzles operating with heated air. Calculated throat heat-transfer coefficients for the 60° half-angle of convergence nozzle agreed reasonably well with the experimental results; however, a gross overprediction (by nearly a factor of 2) resulted when the correlation was applied to the 30° half-angle of convergence nozzle.

Another recent study, which qualitatively illustrates the inadequacies inherent in a correlation approach, is described in reference 6. Results obtained in a center-body experiment at sonic conditions revealed a large difference in friction coefficient for the same throat Reynolds number based on diameter. This difference in friction coefficient was obtained by altering the nozzle geometry. Through Reynolds analogy, a similar effect on the heat transfer would be expected.

A fundamental method of calculating the nozzle heat-transfer coefficients is presented in reference 4. This method involves the simultaneous solution of the integral momentum and energy equations in conjunction with Coles friction law and a modified von Kármán momentum-heat analogy. Application of this boundary-layer theory to air nozzle data in references 3 to 5 yielded better agreement with experimental peak heat-transfer coefficients than predictions based on correlation techniques. The radical difference in convergence angle of the various nozzles provided a rather severe test for the boundary-layer analysis since the relative flow histories in terms of the turning and pressure gradient were appreciably different.

The present experimental study was conducted to further assess the influence of inlet conditions on the heat transfer in 30° and 60° half-angle of convergence nozzles; however, in contrast to the experiment of reference 5, the diameter rather than the length of the uncooled pipe inlets was altered. Inlets having diameters of 6.50, 3.07 and 2.47 inches (16.51, 7.80, and 6.27 cm) corresponding to contraction area ratios of approximately 18.9, 4.2, and 2.7, respectively, were used in the investigation. All tests were conducted with air at a nominal stagnation temperature of 970° R (539° K). Nominal stagnation pressures were 160 and 300 pounds per square inch (110 and 207 N/cm^2) absolute. Experimental nozzle heat-transfer coefficients are compared to calculated values based on (1) the boundary-layer analysis of reference 4, (2) an energy calculation (ref. 7) which was derived as a limiting case of the theory of reference 4, and (3) a Nusselt number correlation.

SYMBOLS

A	area
b	diameter of insulating void surrounding heat-flux meters
$\mathscr{C}_1, \mathscr{C}_2, \mathscr{C}_3$	constants
c	exponent of Reynolds number in skin-friction law
c_f	skin-friction coefficient
$\bar{c}_f$	low-speed adiabatic skin-friction coefficient
c_p	specific heat of air at constant pressure
D	local diameter
$f(T_w/T_s)$	film-temperature function
h	heat-transfer coefficient
i	enthalpy
Δi	enthalpy difference, $i_{ad} - i_w$
$\overline{\Delta i}$	enthalpy difference, $i_0 - i_w$
K	thermal conductivity of Inconel
k	thermal conductivity of air
M	Mach number
Nu	Nusselt number
n	interaction exponent
P	pressure
Pr	Prandtl number
q	local heat flux
Re	Reynolds number
r	radius
St	Stanton number
s	distance along wall
T	temperature
t	temperature on heat-flux meter
u	velocity at edge of boundary layer

x axial coordinate measured from nozzle throat

$\bar{x}$ length of inlets

Y distance along heat-flux meter measured from gas-side wall

z axial coordinate measured from nozzle entrance

$\bar{z}$ axial distance from nozzle entrance to throat

α constant in skin-friction law

β angular position of nozzle instrumentation (tables I and II)

Δ temperature thickness of boundary layer

δ velocity thickness of boundary layer

ϵ_c contraction area ratio

θ momentum thickness of boundary layer

μ viscosity

ρ gas density at edge of boundary layer

φ energy thickness of boundary layer

Subscripts:

ad adiabatic wall condition

D based on diameter

i based on enthalpy

in incompressible

p peak value

r reference condition

s static condition at edge of boundary layer

t throat

w wall condition

θ based on momentum thickness

φ based on energy thickness

0 stagnation condition

APPARATUS

The nozzle heat-transfer facility comprises the following components: (1) a heat exchanger, (2) plenum and bypass flow control system, (3) uncooled pipe inlet, (4) water-cooled nozzle, and (5) an exhaust system. The facility, which was the same as that of references 3 and 5, is shown schematically in figure 1.

Heat Exchanger

The hot gas ejected from a jet-engine burner section was used to heat a series of 1-inch-diameter (2.5-cm-diam) Inconel coils through which passed high-pressure dry air. The dry air was heated to a temperature of about 970° R (539° K) at pressures of 160 and 300 pounds per square inch (110 and 207 N/cm^2) absolute.

Plenum and Bypass Flow Controller

The plenum consisted of a 6-foot-long (1.83-m-long) chamber having entrance and exit diameters of 14.0 and 8.4 inches (35.6 and 21.3 cm), respectively. A Pitot pressure probe having an inside diameter of 0.186 inch (0.472 cm) was positioned on the centerline of the plenum. This probe provided a reference pressure for the manometer system used to measure nozzle static pressures.

A flow bypass manifold, coupled to the downstream end of the plenum, was used to control the velocity profile upstream of the pipe inlets by removing the boundary layer along the plenum wall. Bleed flow rates were adjusted by means of a pneumatically controlled valve operating in a critical flow mode.

Uncooled Pipe Inlets

Uncooled (adiabatic) pipe inlets having inside diameters of 6.50, 3.07, and 2.47 inches (16.51, 7.80, and 6.27 cm) and lengths of 17.0, 18.0, and 18.1 inches (43.2, 45.7, and 46.0 cm), respectively, were used in this investigation. These inlets provided nozzle contraction area ratios of approximately 18.9, 4.2, and 2.7, respectively. Details of the inlet geometries are shown in figure 2. All three inlets were used in conjunction with a 30° half-angle of convergence nozzle; however, only the 6.50- and 3.07-inch-diameter (16.51- and 7.80-cm-diam) inlets were tested with a 60° half-angle of convergence nozzle. All the inlets were machined from AISI 304 stainless-steel pipe

to a wall thickness of 0.25 inch (0.64 cm) and an inside surface finish of 64 micro-inches (1.63 μm) (rms). A thin film of silicone rubber was applied to the downstream end of the inlets to minimize the heat conduction from the water-cooled nozzles. Silicone rubber was also used to seal the 3.07- and 2.47-inch-diameter (7.80- and 6.27-cm-diam) inlets in the supporting chamber as noted in figures 2(b) and (c).

Water-Cooled Nozzles

Two water-cooled conical nozzles, each having a nominal throat diameter and throat radius of curvature of 1.5 inches (3.8 cm) were used in this investigation. The nozzles had a half-angle of convergence of 30° and 60° and a half-angle of divergence of 15° (hereafter these nozzles will be identified by their half-angles). The nozzles were machined from AISI 304 stainless-steel forged billets and had a wall thickness of 0.5 inch (1.3 cm). Cooling water was directed from the downstream to the upstream end of the nozzles by means of lucite shrouds.

Coordinates for the 30°-15° and 60°-15° nozzles are presented in tables I and II, respectively. The expansion ratios for the 30°-15° and 60°-15° nozzles, given by the ratio of exit to throat area, were 25.3 and 3.32, respectively. The exact contraction area ratios corresponding to the various diameter pipe inlets were 18.98, 4.23, and 2.74 for the 30°-15° nozzle and 18.80 and 4.19 for the 60°-15° nozzle.

Exhaust System

The nozzles were connected to a 24-inch-diameter (61-cm-diam) exhaust duct by a thin flexible flange or metallic bellows which yielded to thermal expansion. The exhaust pressure, nominally 2 pounds per square inch (1.4 N/cm^2) absolute, was sufficient to prevent nozzle flow separation as confirmed by the measured static pressure at the last station in the nozzles.

INSTRUMENTATION

Local heat-transfer rates and wall static pressures were measured at stations 2 to 20 in the 30°-15° nozzle and at stations 2 to 16 in the 60°-15° nozzle as noted in tables I and II, respectively. Nozzle wall temperatures were obtained at each of these stations.

Pressures

Nozzle wall static-pressure taps having a diameter of 0.031 inch (0.079 cm) were coupled to manometers which contained mercury, acetylene tetrabromide, and dibutyl phthalate, each selected to give maximum sensitivity in a given Mach number range. In the inlet and nozzle entrance region where differences between the static and total pressure were small, the manometers were connected in a differential fashion and were referenced to the total pressure. This manometer coupling technique provided sufficient accuracy to detect the presence of an adverse pressure gradient in the entrance region. Manometer reference pressures were measured with Bourdon tube gages. Fluid temperature corrections were applied in the reduction of the manometer data.

Heat-Flux Meter

Steady-state measurements of the gas-side wall temperature and local heat-transfer rates were obtained by means of an Inconel plug-type heat-flux meter described in reference 8. The diameter of the plug, shown in figure 3, was the same for the two nozzles. Three Chromel-Alumel 0.003-inch (0.008-cm) wire thermocouples were spot-welded to the 0.125-inch-diameter (0.318-cm-diam) Inconel plug in an inert gas environment. The thermocouple spacing was determined to the nearest 0.001 inch (0.003 cm) by a microscope. The heat-flux meters were installed with a push fit at the gas side of the nozzle and a high temperature O-ring seal at the water-cooled side. A stagnant air column surrounding the plug provided the thermal insulation necessary for one-dimensional heat conduction through the shaft. Each heat-flux meter was located 180° from the static pressure tap in the same axial plane as noted in tables I and II for the 30°-15° and 60°-15° nozzles, respectively.

DATA REDUCTION

Local Heat-Flux and Wall Temperature

Temperatures measured on the Inconel heat-flux meter were incorporated in the Fourier heat conduction equation to determine both the gas-side wall temperature and the local heat-transfer rate per unit area. This equation is

$$q = -K(t) \frac{dt}{dY}$$

where the thermal conductivity K of the Inconel can be represented to within about ±2 percent over the desired temperature range by the following linear relation:

$$K = 1.307\times10^{-7}\, t(^{o}F) + 1.704\times10^{-4}\ \text{Btu/(sec)(in.)}(^{o}F)$$

or

$$K = 1.758\times10^{-4}\, t(^{o}K) + 8.243\times10^{-2}\ \text{W/(cm)}(^{o}K)$$

Integration of the Fourier equation yields a temperature distribution along the Inconel plug of the following form:

$$-qY = \mathscr{C}_1 t^2 + \mathscr{C}_2 t + \mathscr{C}_3$$

The unknowns q and $\mathscr{C}_3$ were determined by the simultaneous solution of two equations containing the measured temperature t and the corresponding location Y at two of the three stations along the heat-flux meter. Wall temperatures were computed by setting Y = 0.

Measurement of three temperatures along the meter shaft provided three possible combinations for computing the nozzle wall temperature. In approximately 95 percent of the readings, the average value of the three wall temperatures was used in the subsequent calculation of the local heat-transfer coefficient. Defective thermocouples necessitated the computation of the wall temperature from a single pair of thermocouples in the remaining 5 percent of the readings.

Error Considerations

The measured heat fluxes in this investigation, as in reference 3, were estimated to be no more than 10 percent higher than the true one-dimensional values. This 10-percent uncertainty factor, which is due to the void around the heat-flux meter, does not apply to the wall temperature. Direct measurements of the peak wall temperature by means of Chromel-Alumel thermocouples agreed to within 1 percent of the absolute temperature computed from plug measurements. As a matter of consistency, all experimental heat-transfer coefficients will be presented as computed from the direct measurement of one-dimensional heat flux; however, in certain comparisons of the data to various predictions, a 10-percent conduction uncertainty band will be attached to the peak heat-transfer coefficient. Experimental inaccuracies in heat flux resulting from errors in (a) plug temperatures, (b) thermocouple spacing, and (c) the thermal conductivity of the Inconel are less than ±3 percent and, therefore, for purposes of this

investigation have been considered negligible. Errors in experimental heat flux resulting from (1) the relative difference in the thermal conductivity of the stainless-steel nozzle and the Inconel plugs and (2) the effects of wall curvature have also been neglected.

PROCEDURE

Tests were conducted at nominal stagnation pressures of 160 and 300 pounds per square inch (110 and 207 N/cm^2) absolute at a stagnation temperature of 970° R (539° K). While approaching the desired operating conditions, the bleed flow rate was adjusted until the plenum boundary layer was removed as confirmed by a mean velocity profile obtained with a hot wire upstream of the 6.50-inch-diameter (16.51-cm-diam) pipe inlet. The same bleed flow rate was established for all inlet configurations.

All temperature and pressure data were obtained in a period of 15 minutes. Temperatures were recorded 10 times by an automatic voltage digitizer in order to verify the presence of steady-state operating conditions and to permit the averaging of small recording errors. The Bourdon tube reference pressure gages were read, and the manometers were photographed 2 to 4 times in the 15-minute recording interval.

EXPERIMENTAL RESULTS

Nozzle-Pressure Distribution

Experimental and one-dimensional static- to total-pressure ratios P_s/P_0 for the nozzles are tabulated in table III. Also shown are the pressure ratios for the uncooled pipe inlets; however, static pressures were measured only in the 6.50-inch-diameter (16.51-cm-diam) inlet. One-dimensional values of pressure ratio were used in calculating the boundary-layer development in the 3.07- and 2.47-inch-diameter (7.80- and 6.27-cm-diam) inlets.

The measured pressure ratios deviated considerably from the one-dimensional values in the throat region of the nozzle as was also observed in references 9 and 10. In addition, static-pressure measurements indicated the presence of an adverse pressure, gradient in the corner formed by the intersection of the 6.50-inch-diameter (16.51 cm-diam) inlet and the nozzles (table III, inlet and station 2). Similar observations were made in reference 10 for a cylindrical inlet and conical nozzle intersection having a slight radius of curvature rather than a sharp corner as in the present investigation. The pressures tabulated in table III also indicate that the adverse gradient terminates and again becomes favorable between stations 2 and 3 in the nozzle or at a distance along

the wall of less than 1.4 inches (3.6 cm) from the nozzle entrance. In the case of the smaller diameter inlets, the presence of an adverse gradient could not be detected with the existing instrumentation.

Heat-Transfer Distributions in the Nozzles

In this section the experimental heat-transfer distributions, presented in figures 4 to 8, are discussed. Three distributions, representing predicted results, are also shown in this series of figures; however, discussion of the predicted heat transfer will be deferred to the succeeding section. The experimental results have been duplicated in figures 9 to 13 for purposes of clarity in comparisons with additional theoretical curves.

Experimental heat-transfer distributions will be presented in terms of the heat-transfer coefficient based on enthalpy which is given by the following equation:

$$h_i = \frac{q}{i_{ad} - i_w}$$

where the adiabatic enthalpy was given by

$$i_{ad} = i_s + Pr^{1/3}(i_0 - i_s)$$

The Prandtl number was assumed constant at 0.71. Static and total enthalpies i_s and i_0, respectively, were computed using the equations of reference 11 for enthalpy, and specific heat in conjunction with an assumed isentropic expansion process. Heat-transfer coefficients will be plotted as a function of the axial distance from the nozzle entrance z; therefore, caution should be exercised in comparing results for different inlet diameters on the basis of the same value of z. The relation between z and the axial distance from the nozzle throat x can be obtained from tables IV and V which contain the experimental values of h_i and T_w, respectively, for all the configurations and stagnation conditions investigated. Experimental values of h_i are plotted as a function of axial distance for the 30^o-15^o nozzle with the 6.50-, 3.07-, and 2.47-inch-diameter (16.51-, 7.80-, and 6.27-cm-diam) inlets in figures 4, 5, and 6, respectively, and for the 60^o-15^o nozzle with the 6.50- and 3.07-inch-diameter (16.51- and 7.80-cm-diam) inlets in figures 7 and 8, respectively. Distributions of h_i are presented for each configuration at nominal stagnation pressures of 300 and 160 pounds per square inch (207 and 110 N/cm^2) absolute corresponding to parts a and b, respectively, in each figure.

As mentioned previously, the plenum boundary-layer bleed flow rate was the same for all inlet configurations. This flow rate was sufficient to remove the plenum boundary layer and establish a uniform velocity profile across the 6.50-inch-diameter (16.51-cm-diam) inlet. However, in order to establish the effect of possible secondary flows ahead of the 3.07- and 2.47-inch-diameter (7.80- and 6.27-cm-diam) inlets resulting from the method of installation of the smaller inlets (fig. 2), tests were repeated with a zero bleed-flow rate. Measured heat-transfer rates with no bleed flow were the same as the values obtained with the bleed flow incorporated. Further evidence of this insensitivity of nozzle heat transfer to upstream flow conditions is presented in references 3 and 5.

In all tests a reduction in stagnation pressure for other conditions remaining fixed resulted in a lower heat-transfer distribution as expected. If at a given station h_i is assumed to vary as the mass flux to a power $h_i \alpha (\rho u)^{0.8}$, a decrease in stagnation pressure of from 300 to 160 pounds per square inch (207 to 110 N/cm^2) absolute would produce a reduction of 40 percent in h_i. Experimentally, the reduction in the peak value of h_i was between 29 and 47 percent where these limits correspond to the 6.50-inch-diameter (16.51-cm-diam) inlet coupled to the 30°-15° and 60°-15° nozzles, respectively, (refer to figs. 4 and 7).

Comparison of figures 4 to 6 for the 30°-15° nozzle with figures 7 and 8 for the 60°-15° nozzle reveals that a reduction in the uncooled pipe inlet diameter produced an appreciable increase in the peak value of h_i. In the 30°-15° nozzle operating at 300 pounds per square inch (207 N/cm^2) absolute, an increase of 72 percent is the peak value of h_i was obtained for a reduction in inlet diameter of from 6.50 to 3.07 inches (16.51 to 7.80 cm) (figs. 4 and 5). The maximum value of h_i obtained in this study was with the smallest inlet which had a diameter of 2.47 inches (6.27 cm) (fig. 6). This maximum value was 110 percent higher than the peak value of h_i for the configuration having an inlet diameter of 6.50 inches (16.51 cm).

In the 60°-15° nozzle operating at 300 pounds per square inch (207 N/cm^2) absolute, an increase of 45 percent in the peak value of h_i was obtained when the inlet diameter was reduced from 6.50 to 3.07 inches (16.51 to 7.80 cm) (figs. 7 and 8, respectively). The same trends of higher heat transfer with lower inlet diameter were apparent for both nozzles at the lower stagnation-pressure level.

Experimental peak values of h_i were consistently higher in the 60°-15° nozzle for the same inlet and stagnation conditions. A comparison of figures 4 and 7 shows the peak value of h_i in the 60°-15° nozzle was about 47 percent higher than the value in the 30°-15° nozzle when operating with the 6.50-inch-diameter (16.51-cm-diam) inlet at a stagnation pressure of 300 pounds per square inch (207 N/cm^2) absolute. Similar differences in the 30°-15° and 60°-15° nozzle peak values of h_i were apparent for the 3.07-inch-diameter (7.80-cm-diam) configuration and also for the lower stagnation-pressure operating condition.

COMPARISON OF EXPERIMENTAL AND PREDICTED HEAT-TRANSFER COEFFICIENTS

In this section, experimental heat-transfer distributions are compared to the results based on (1) a Nusselt number correlation, (2) the boundary-layer theory of reference 4, and (3) an energy calculation method generated from the boundary-layer theory. In figures 4 to 8, results are given for the Nusselt number correlation as well as the boundary-layer theory in which the diabatic skin-friction coefficient was assumed equal to the adiabatic value. In figures 9 to 13, the experimental heat-transfer distributions are repeated and are compared to predictions based on the energy calculation method and the boundary-layer theory in which the diabatic skin-friction coefficient was assumed equal to the product of the low-speed adiabatic value and a film-temperature correction factor. Examples of the effects of the static-pressure distribution and interaction exponent on the heat transfer calculated from the boundary-layer theory are given in figures 14 and 15, respectively. Finally, in figure 16, the experimental and the predicted peak heat-transfer coefficients are compared on the basis of nozzle contraction ratio.

Nusselt Number Correlation

The experimental heat-transfer coefficients are compared to a simple pipe-flow type of correlation herein referred to as a Nusselt number correlation given by

$$Nu_r = 0.026\ Re_{D,r}^{0.8}\ Pr^{1/3}$$

where the subscript r indicates that the flow properties are evaluated at the Eckert reference enthalpy condition (ref. 12). The Prandtl number Pr was assumed constant, 0.71, and the Reynolds number $Re_{D,r}$ based on the local diameter of the nozzle is given by

$$Re_{D,r} = \frac{\rho_r u D}{\mu_r}$$

Heat-transfer coefficients were calculated from the Nusselt number according to the following equation:

$$h_i = \frac{k_r Nu_r}{C_{p,r} D}$$

Heat-transfer distributions based on this Nusselt number correlation are presented in figures 4 to 8. The maximum deviation from the experimental peak value of h_i occurred with the 30^o-15^o nozzle operating with the 6.50-inch-diameter (16.51-cm-diam) inlet at a stagnation pressure of 300 pounds per square inch (207 N/cm^2) absolute. In this case, the Nusselt number correlation overpredicted the peak value of h_i by nearly 84 percent (fig. 4(a)). At the lower stagnation pressure, the Nusselt number correlation overpredicted the peak value of h_i by about 55 percent (fig. 4(b)). An appreciable overprediction in the peak value of h_i can also be noted in figure 7 for the 60^o-15^o nozzle operating with the same inlet. For the other nozzle-inlet combinations, presented in figures 5, 6, and 8, the agreement with the experimental peak values of h_i was much better with a maximum overprediction of 6 percent and a maximum underprediction of 15 percent (figs. 5(a) and 8(a), respectively).

Boundary-Layer Theory

Experimental values of h_i have been compared to predictions based on the turbulent boundary-layer theory of reference 4. The method essentially involves the solution of the integral momentum and energy equations and employs Coles friction law, 1/7-power profiles for velocity and temperature difference, and the von Kármán form of Reynolds analogy. Reference 4 should be consulted for details of the assumptions incorporated in this method. Two basic options, provided in this boundary-layer program, concern the selection of an interaction exponent and method of evaluating the diabatic skin-friction coefficient.

Interaction exponent option. - The first option concerns the selection of an exponent n called the interaction exponent which is used to relate the Stanton number for unequal momentum and energy thicknesses to that for equal thicknesses by means of a factor $(\varphi/\theta)^n$. In the present investigation the interaction exponent was assumed to be zero unless specified.

Skin-friction option. - The second option deals with the method of evaluating the diabatic skin-friction coefficient c_f. One of the methods of determining c_f was to assume that it was equal to the adiabatic skin-friction coefficient $c_{f,ad}$ obtained when $T_w = T_{ad}$. The value of $c_{f,ad}$ was based on free-stream gas properties.

A second method of determining c_f incorporates a film-temperature correction factor which is applied to the low-speed value of $c_{f,ad}$ (denoted by $\bar{c}_f$) according to the following relation:

$$c_f = f\left(\frac{T_w}{T_s}\right)\bar{c}_f = \left[\frac{1}{2}\left(\frac{T_w}{T_s} + 1\right)\right]^{-0.587} \bar{c}_f$$

The value of $c_{f,ad}$ or $\bar{c}_f$ was determined by a method of Coles (ref. 13) which gives $c_{f,ad}$ as a function of Mach number M and the momentum thickness Reynolds number Re_θ. Details of the calculation procedure are given in reference 4.

Boundary-layer initialization. - The boundary-layer calculation of the nozzle heat transfer requires initialization with respect to the momentum thickness θ and the ratio of thermal to velocity layer thickness $(\Delta/\delta)_{z=0}$. Since the inlets were uncooled, only the momentum thickness development in the pipes was considered. In all calculations involving a zero interaction coefficient, the heat-transfer is independent of the value of $\theta_{z=0}$; however, because of the programming technique $\theta_{z=0}$ was a required input variable. Estimates of the value of $\theta_{z=0}$ were obtained from the following equation:

$$\theta_{z=0} \approx 0.04\, \bar{x}\, Re_{\bar{x}}^{-1/5}$$

where $\bar{x}$ was the length of the inlet, and the constant, 0.04, was obtained from the boundary-layer measurements of references 2 and 5.

The boundary-layer calculation was reinitiated at the nozzle entrance using the calculated value of $\theta_{z=0}$ and an assumed value of $(\Delta/\delta)_{z=0}$. In order to determine the sensitivity of the assumed value of $(\Delta/\delta)_{z=0}$ on the peak value of h_i, a range of values of from 0.005 to 1.0 were incorporated in the program. The peak value of h_i was rather sensitive to the value of $(\Delta/\delta)_{z=0}$ in the range of 0.1 to 1.0; however, values in this range were considered too large in view of the adiabatic inlet condition which caused the thermal boundary layer to begin at the nozzle entrance. The value of Δ/δ at this station was expected to be quite small, that is, $\Delta \ll \delta$. For values of $(\Delta/\delta)_{z=0} < 0.1$, the peak value of h_i rapidly approached an asymptotic value. A lower value of $(\Delta/\delta)_{z=0}$ equal to 0.01 was used in the calculations because it ensured convergence to the asymptotic peak heat-transfer coefficient within a practical computing time.

Heat-transfer distributions. - The results of the boundary-layer calculation of nozzle heat transfer are presented in figures 4 to 8 for assumed values of $(\Delta/\delta)_{z=0}$ equal to 0.01 and 1.0. In this series of calculations, $c_f = c_{f,ad}$ corresponds to free-stream gas properties. Results are presented for the two values of $(\Delta/\delta)_{z=0}$ to indicate the sensitivity of this assumption on the calculated values of h_i; however, as stated previously, the value of $(\Delta/\delta)_{z=0} = 0.01$ is expected to better represent the actual flow.

An examination of figures 4 to 8 indicates that the calculated heat-transfer distribution was higher for the lower of the two assumed values of $(\Delta/\delta)_{z=0}$. Also, a comparison of figure 4 with figure 6 for the 30°-15° nozzle and figure 7 with figure 8 for the 60°-15°

nozzle reveals that the effect of $(\Delta/\delta)_{z=0}$ on the peak value of h_i was greater for the small diameter inlets (low contraction ratio configurations). In general, the best agreement between theoretical and experimental peak values of h_i was obtained with $(\Delta/\delta)_{z=0}$ equal to 0.01. An exception, however, can be noted for the 30^o-15^o nozzle operating with the 6.50-inch-diameter (16.51-cm-diam) inlet (fig. 4(a)). In this case, the predicted peak value of h_i was nearly 35 percent higher than the experimental value.

The experimental heat-transfer distributions, which have been duplicated in figures 9 to 13, are compared to predictions based on the second option of the skin-friction coefficient. As noted previously, this option assumes $c_f = f(T_w/T_s)\bar{c}_f$. All calculations were based on a value of $(\Delta/\delta)_{z=0}$ equal to 0.01.

Incorporation of this second form of the friction law resulted in a downward displacement of the previously obtained heat-transfer distributions in which $c_f = c_{f,ad}$. This displacement can be noted typically by comparing figure 4 with figure 9 or figure 7 with figure 12 for the 30^o-15^o and 60^o-15^o nozzles, respectively. This second form of the friction law improved the agreement between experimental and theoretical peak values of h_i in the case of the 30^o-15^o nozzle with the 6.50-inch-diameter (16.51-cm-diam) inlet (figs. 4 and 9) and in the case of the 60^o-15^o nozzle with the 6.50-inch-diameter (16.51-cm-diam) inlet (figs. 7(b) and 12(b)). In all the other configurations, the agreement degenerated.

Energy Calculation of Nozzle Heat Transfer

In reference 7, it was shown that for certain assumptions, including one-dimensional flow and a zero interaction exponent, a simple closed form solution of the integral energy equation can be generated. As shown in the appendix, the assumption of one-dimensional flow is unnecessary, and a simplified solution similar to that of reference 7 can be obtained. The expression for Re_φ (eq. (A6)) is

$$(Re_\varphi \mu r \overline{\Delta i})^{1-c} = \frac{(1-c)\alpha}{1.8} \int_{z=0}^{z} \frac{\rho_r}{\rho} \frac{\Delta i}{\overline{\Delta i}} \frac{(Re_{\varphi,r})^c}{\varphi} (Re_\varphi \mu r \overline{\Delta i})^{1-c} \left[1 + \left(\frac{dr}{dz}\right)^2\right]^{0.5} dz$$

$$+ (Re_\varphi \mu r \overline{\Delta i})_{z=0}^{1-c}$$

where α and c are constants in the friction law (eq. (A4)).

A further simplification can be made in the expression for Re_φ if the additional assumptions of an isothermal wall, an enthalpy recovery factor of 1.0, and constant viscosity are made. The equation for Re_φ (eq. (A7)) then becomes

$$(\mathrm{Re}_{\varphi}\ r)^{1-c} = \frac{(1-c)\alpha}{1.8}\int_{z=0}^{z}\frac{\rho_r}{\rho}\frac{(\mathrm{Re}_{\varphi,r})^{c}}{\varphi}(\mathrm{Re}_{\varphi}\ r)^{1-c}\left[1+\left(\frac{dr}{dz}\right)^{2}\right]^{0.5}dz + (\mathrm{Re}_{\varphi}\ r)^{1-c}_{z=0}$$

The expression for h_i (eq. (A8)) in which $\alpha = 0.0258$ and $c = 0.25$ is

$$h_i = 0.0143\,\rho u\,\frac{T_s}{T_r}\,\mathrm{Re}^{-0.25}_{\varphi,r}$$

which can also be expressed in terms of the Nusselt number (eq. (A9)) as follows:

$$\mathrm{Nu}_r = 0.0143\,\mathrm{Re}^{0.75}_{D,r}\,\mathrm{Pr}_r\left(\frac{\varphi}{D}\right)^{-0.25}$$

This expression for the Nusselt number differs from the value in the simple pipe-flow type equation by the factor $0.438\,(\varphi/D)^{-0.25}$.

The results of the energy calculation of nozzle heat transfer obtained from the variable temperature and isothermal wall expressions (eqs. (A6) and (A7), respectively) are presented in figures 9 to 13. In these figures, the isothermal wall designation also implies a recovery factor of 1.0. A comparison of the distributions of heat-transfer coefficients obtained from the two forms of the simple energy calculation shows that the isothermal wall assumption is good for the class of nozzles and the stagnation conditions investigated. The isothermal wall assumption generally produced less than 10 percent higher peak values of h_i than the variable temperature wall form of the equation as noted typically in figures 9 and 12 for the 30°-15° and the 60°-15° nozzles, respectively.

The results of the energy calculation parallel those of the full boundary-layer theory. Peak values of h_i calculated by the energy method, ranged from 16 to 23 percent higher than the values based on the boundary-layer theory. The similar trends in the results are not surprising since the first-order difference between the simplified and the full boundary-layer theory containing a zero interaction exponent are merely the friction law and nonunity Prandtl number correction factor.

Influence of Nozzle-Pressure Ratio on the Calculated Heat Transfer

In practical applications of the boundary-layer theory, it is frequently desirable to use one-dimensional pressure ratios to describe the mass-flux variation in the nozzle. In table III, pronounced deviations from the one-dimensional pressure ratios can be noted

in the form of an adverse gradient in the nozzle entrance and lower values of static pressure in the throat region. The effect of the pressure distribution on the calculated heat transfer thus becomes a primary consideration.

A comparison of the measured pressure ratio P_s/P_0 in the 6.50-inch-diameter (16.51-cm-diam) inlet and station 2 in the 30°-15° and 60°-15° nozzles (table III) indicates the presence of an adverse pressure gradient. Since the magnitude of the pressure difference appeared to be greatest in the 60°-15° nozzle, this configuration was selected for a study of the influence of the adverse pressure gradient on the heat-transfer distribution calculated from the boundary-layer theory of reference 4. The calculated heat-transfer distribution (fig. 7(a)) is compared in figure 14 to the distribution obtained when one-dimensional nozzle-pressure ratios were incorporated in the boundary-layer theory. The greatest influence of nozzle-pressure ratio can be noted at the nozzle entrance where the adverse gradient was present. Here the calculated value of h_i based on one-dimensional pressure ratios was nearly 4 times as great as the value based on the experimental pressure distribution. It is probable that this large difference in calculated heat transfer is partially a reflection of the sensitivity of the mass flux to the experimental pressure ratio. In progressing downstream, the difference in calculated values of h_i rapidly diminishes. The peak value of h_i based on the experimental pressure distribution was only about 5.0 percent higher than the value based on a one-dimensional pressure distribution. In most practical applications, this difference in the peak value of h_i is insignificant thus suggesting that in the absence of an experimental or axisymmetric pressure distribution, one-dimensional values may be used without appreciably influencing the accuracy of the calculated heat transfer in the throat region.

Variation of the Interaction Exponent

In reference 4, the limits for the interaction exponent are given as 0 and 0.25. The effect of various interaction exponents on the calculated heat transfer is shown typically in figure 15. Heat-transfer distributions, corresponding to interaction coefficients of 0, 0.10, and 0.25, have been calculated for the 30°-15° nozzle operating with the 6.50-inch-diameter (16.51-cm-diam) inlet at a stagnation pressure of 299.5 pounds per square inch (206.5 N/cm^2) absolute. The calculations were performed using the adiabatic form of the friction coefficient corresponding to free-stream gas properties. A pronounced increase in peak heat-transfer coefficient accompanied the increase in interaction exponent. The peak value of h_i based on an interaction exponent of 0.25 was 65 percent higher than the value obtained with a zero interaction exponent. In this case, the zero interaction exponent produced the best agreement between the experiment and theory. In cases where the theory underpredicted the experimental peak value of h_i (figs. 5, 6, and 8)

incorporation of a nonzero interaction exponent would effect only a slight improvement in the agreement; therefore, within the scope of the present tests, the assumption of a zero interaction exponent appears reasonable.

PEAK HEAT-TRANSFER DEPENDENCE ON CONTRACTION AREA RATIO

In figure 16, experimental and calculated peak heat-transfer coefficients $h_{i,p}$ are plotted as a function of contraction area ratio ϵ_c. The four experimental fairings are indicative of the heat-transfer variation with contraction area ratio for the 30°-15° and 60°-15° nozzles, each operating at a stagnation temperature of about 970° R (539° K) and nominal stagnation pressures of 160 and 300 pounds per square inch (110 and 207 N/cm^2) absolute. A 10-percent experimental uncertainty band has been applied to the data for, as mentioned previously, heat conduction resulting from the presence of an insulating void around the heat meter could effect an increase in the measured heat-transfer rates.

In figure 16, a substantial increase in the experimental values of $h_{i,p}$ with reduced values of ϵ_c (smaller inlet diameter) can be observed for both nozzles and stagnation pressure levels. In the 30°-15° nozzle operating at the high-pressure level (fig. 16(a)) an increase of 72 percent in $h_{i,p}$ was obtained (assuming the same relative experimental errors) for a reduction in ϵ_c of from 19.0 to 4.2. The maximum value of $h_{i,p}$, obtained with the minimum value of ϵ_c (2.7), was about 110 percent higher than the value of $h_{i,p}$ for ϵ_c equal to 19.0. A similar increase in $h_{i,p}$ can be noted at the lower pressure level (fig. 16(b)).

Results for the 60°-15° nozzle operating at the high stagnation-pressure level (fig. 16(a)) indicate that an increase in $h_{i,p}$ of 45 percent occurred when the value of ϵ_c was reduced from 18.8 to 4.2. The corresponding increase in $h_{i,p}$ at the low stagnation-pressure level was 55 percent (fig. 16(b)). Again, these numbers are premised on the assumption of the same relative experimental errors.

A pronounced difference between the calculated and the experimental variations of $h_{i,p}$ with ϵ_c can be noted in figure 16. Values of $h_{i,p}$ calculated from the Nusselt number correlation were totally invarient with ϵ_c and convergence angle for given stagnation conditions; however, a pronounced increase in $h_{i,p}$ with decreasing ϵ_c was obtained experimentally. The constant values of $h_{i,p}$ calculated from the correlation equation are the result of nearly equal throat mass fluxes and diameters for all values of ϵ_c. The influence on the calculated values of h_i resulting from differences in the local reference temperatures was negligible. In all cases except for the 30°-15° nozzle having a contraction area ratio of 4.2, a pronounced overprediction (by nearly a factor of 2 at

the high value of ϵ_c) or modest underprediction can be noted for the Nusselt number correlation.

The results of the boundary-layer theory shown in figure 16 indicate the experimentally observed trend of increasing $h_{i,p}$ with decreasing ϵ_c; however, the rates at which $h_{i,p}$ increases, denoted by the slopes of the curves, are not consistent with the measurements. Also, for equal values of ϵ_c the boundary-layer theory fails to predict correctly the difference in $h_{i,p}$ in the two nozzles operating at 300 pounds per square inch (207 N/cm^2) absolute. At the lower stagnation pressure of 160 pounds per square inch (110 N/cm^2) absolute, the experimental difference in $h_{i,p}$ for the two nozzles at a given value of ϵ_c is within the theoretical predictions only if an uncertainty factor of 10 percent is applied to the 60°-15° nozzle data. On the basis of absolute rather than relative levels of heat transfer, the largest discrepancy between experimental and theoretical values of $h_{i,p}$ occurred in the case of the 30°-15° nozzle having a contraction area ratio of 19.0; however, this difference from the experimental value was much less than the corresponding difference arising from the Nusselt number correlation. In view of the uncertainties associated with the theoretical assumptions, initialization technique, and experiment, the boundary-layer theory is considered to show the effect of contraction ratio reasonably well.

The boundary-layer predictions of $h_{i,p}$ shown in figure 16 are essentially representative of the values obtained by the simple energy calculation technique; however, for the purpose of clarity, the results from the energy calculation are not presented in this figure. An indication of the ability of the energy calculation to comprehend the contraction ratio effect on $h_{i,p}$ can be obtained by comparing, for instance, figure 9 with figure 11, which correspond to the 30°-15° nozzle having contraction ratios of 19.0 and 4.2, respectively.

SUMMARY OF RESULTS

An experimental investigation has been performed in order to assess the effect of a variation in uncooled pipe inlet diameter and the associated contraction area ratio of the heat transfer in conical nozzles having 30° and 60° half-angles of convergence. Additionally, three calculation methods were applied in an attempt to predict the heat transfer, with particular emphasis on the throat region of the nozzles. These methods included (1) an integral boundary-layer analysis, (2) an energy calculation technique derived from the boundary-layer theory, and (3) a Nusselt number pipe-flow type of correlation. Measurements were obtained at nominal stagnation pressures of 160 and 300 pounds per square inch (110 and 207 N/cm^2) absolute. All tests were performed at a nominal stagnation temperature of 970° R (539° K). The principal results of this investigation are as follows:

(1) Substantial increases in the peak heat-transfer coefficient accompanied a reduction in contraction area ratio (smaller inlet diameters) when uncooled pipe inlets are used with cooled conical nozzles.

(2) The simple Nusselt number correlation, in which the heat-transfer coefficient is primarily a function of the Reynolds number based on the local diameter, was only able to predict the peak heat transfer for certain combinations of inlets and nozzles. In some cases, the correlation equation produced nearly a 100 percent overprediction of the peak heat-transfer coefficient. The correlation method did not comprehend the experimentally observed convergence angle and contraction area ratio effects on the nozzle heat transfer.

(3) For the conditions investigated, the integral boundary-layer theory yielded a fair prediction of the nozzle heat transfer. A comprehension of convergence angle and contraction area ratio effects was evident although not to a degree consistent with the experimental results. In general, the integral boundary-layer approach was better than the Nusselt number correlation.

(4) An approximate formulation of the boundary-layer theory, in which the energy equation was solved exclusive of the momentum equation, produced results consistent with those obtained with the general boundary-layer theory.

CONCLUDING REMARKS

The observed changes in the nozzle throat turbulent heat-transfer rates accompanying the alterations in inlet diameter or nozzle convergence angle are expected to be predominantly due to changes in the acceleration history of the thermal boundary layer which commenced at the nozzle entrance. In reference 5, experimental results indicated a negligible influence of inlet momentum history on the throat heat flux; however, unlike the momentum consideration, the inlet thermal history is expected to contribute to the turbulent transport of heat in the nozzle. Therefore, caution should be exercised in extrapolating the present results to configurations in which cooled inlets are employed.

Since predictions of the nozzle heat transfer from the energy calculation method and the integral boundary-layer theory of reference 4 were in good agreement, the simpler energy method is recommended for estimates of nozzle heat transfer or thermal boundary-layer characteristics. However, it is important to recognize that in applications of the energy method, a knowledge of the initial thermal boundary-layer thickness is required. In configurations amenable to this type of initialization, the energy method

is recommended in preference to the Nusselt number correlation for calculations of the nozzle heat transfer.

Lewis Research Center,
National Aeronautics and Space Administration,
Cleveland, Ohio, May 22, 1967,
129-01-09-06-22.

APPENDIX - ENERGY CALCULATION OF NOZZLE HEAT TRANSFER

The assumptions presented in reference 4, when combined with (1) a zero interaction exponent, (2) an approximation for the nonunity Prandtl number term in the modified von Kármán form of the Reynolds analogy and (3) a Blasius friction law in which c_f is evaluated at $\varphi = \theta$ are sufficient to provide a simple closed form solution of the energy equation (ref. 7).

In reference 4, the Stanton number was computed from a modified von Kármán form of Reynolds analogy given by

$$St = \frac{\frac{c_f(Re_\varphi)}{2}\left(\frac{\varphi}{\theta}\right)^n}{1 - 5\left[\frac{c_f(Re_\varphi)}{2}\right]^{0.5}\left[1 - Pr + \ln\left(\frac{6}{5\,Pr + 1}\right)\right]} \tag{A1}$$

where the interaction coefficient $(\varphi/\theta)^n$ is a correction factor for unequal momentum and energy thicknesses. For the special case of $n = 0$, the integral energy equation can be completely divorced from the momentum equation thus providing the basis for the closed form solution of the nozzle heat transfer. The equations for the nozzle heat transfer (which differ slightly from those of ref. 7) are derived herein.

The integral energy equation for axisymmetric flow can be written as follows:

$$\frac{q}{r\rho u_\varphi \overline{\Delta i}} = \frac{1}{r}\frac{d}{ds} \ln \rho u r \overline{\Delta i}\, \varphi = \frac{St}{r\varphi}\left(\frac{\Delta i}{\overline{\Delta i}}\right) \tag{A2}$$

where $\Delta i = i_{ad} - i_w$ and $\overline{\Delta i} = i_0 - i_w$.

The denominator of equation (A1) involves a function of Pr and c_f which, for a nozzle, has a weak axial dependence. This denominator was assumed constant at a mean value of 0.9. Incorporation of this constant in equation (A2) yields

$$\frac{d}{ds} \ln \rho u r \overline{\Delta i}\, \varphi = \frac{c_f(Re_\varphi)}{1.8\,\varphi}\left(\frac{\Delta i}{\overline{\Delta i}}\right) \tag{A3}$$

The Blasius form of the skin-friction coefficient, evaluated on the basis of $\varphi = \theta$, will be incorporated in equation (A3). This friction law can be expressed as follows:

$$c_{f,in} = \alpha\, Re_\varphi^c$$

where α and c are constants, and $c_{f,in}$ is the incompressible value of the friction coefficient. As noted in reference 14, the compressible form of the friction law can be written in terms of the Eckert reference temperature as

$$c_f = \frac{\rho_r}{\rho} (c_{f,in})_r$$

where, in this analysis,

$$(c_{f,in})_r = \alpha \, Re^c_{\varphi, r}$$

Therefore,

$$c_f = \alpha \frac{T_s}{T_r} Re^c_{\varphi, r} \tag{A4}$$

where $\alpha = 0.0258$, and $c = -0.25$. Substitution of equation (A4) into equation (A3) yields the final differential equation for φ, which is

$$(\rho u r \varphi \, \overline{\Delta i})^{1-c} \frac{d}{ds} \ln \rho u r \varphi \, \overline{\Delta i} = \frac{T_s}{T_r} \frac{\alpha}{1.8} \left(\frac{Re_{\varphi, r}}{\varphi} \right)^c \frac{\Delta i}{\overline{\Delta i}} (\rho u r \, \overline{\Delta i})^{1-c} \tag{A5}$$

Equation (A5) can be readily integrated to give the following equation for the Re_φ distribution in the nozzle:

$$(Re_\varphi \, \mu r \, \overline{\Delta i})^{1-c} = \frac{(1-c)\alpha}{1.8} \int_{z=0}^{z} \frac{\rho_r}{\rho} \frac{\Delta i}{\overline{\Delta i}} \frac{(Re_{\varphi, r})^c}{\varphi} (Re_\varphi \, \mu r \, \overline{\Delta i})^{1-c} \left[1 + \left(\frac{dr}{dz} \right)^2 \right]^{0.5} dz$$

$$+ (Re_\varphi \, \mu r \, \overline{\Delta i})^{1-c}_{z=0} \tag{A6}$$

It should be noted that the integrand in equation (A6) is not a function of φ.

In the special case of an isothermal wall, an assumed enthalpy recovery factor of 1.0, and constant viscosity, equation (A6) reduces to the following relation:

$$(\mathrm{Re}_{\varphi}\ r)^{1-c} = \frac{(1-c)\alpha}{1.8} \int_{z=0}^{z} \frac{\rho_r}{\rho} \frac{(\mathrm{Re}_{\varphi,r})^c}{\varphi} (\mathrm{Re}_{\varphi}\ r)^{1-c} \left[1 + \left(\frac{dr}{dz}\right)^2\right]^{0.5} dz + (\mathrm{Re}_{\varphi}\ r)_{z=0}^{1-c} \tag{A7}$$

When equation (A6) or equation (A7) are solved for Re_{φ}, the local heat-transfer coefficient can be determined from the assumed form of Reynolds analogy given by

$$h_i = 0.0143\, \rho u \frac{T_s}{T_r} \mathrm{Re}_{\varphi,r}^{-0.25} \tag{A8}$$

Equation (A8) can be expressed alternately in terms of the Nusselt number as follows:

$$\mathrm{Nu}_r = 0.0143\, \mathrm{Re}_{D,r}^{0.75}\, \mathrm{Pr}_r \left(\frac{\varphi}{D}\right)^{-0.25} \tag{A9}$$

REFERENCES

1. Benser, W. A.; and Graham, R. W.: Hydrogen Convective Cooling of Rocket Nozzles. Paper No. 62-AV-22, ASME, June 1962.

2. Schacht, Ralph L.; Quentmeyer, Richard J.; and Jones, William L.: Experimental Investigation of Hot-Gas Side Heat-Transfer Rates for a Hydrogen-Oxygen Rocket. NASA TN D-2832, 1965.

3. Boldman, Donald R.; Schmidt, James F.; and Fortini, Anthony: Turbulence, Heat-Transfer, and Boundary Layer Measurements in a Conical Nozzle with a Controlled Inlet Velocity Profile. NASA TN D-3221, 1966.

4. Elliott, David G.; Bartz, Donald R.; and Silver, Sidney: Calculation of Turbulent Boundary-Layer Growth and Heat-Transfer in Axi-Symmetric Nozzles. Tech. Rep. 32-387, Jet Propulsion Lab., California Inst. Tech., Feb. 1963.

5. Boldman, D. R.; Schmidt, J. F.; and Ehlers, R. C.: Some Effects of Uncooled Pipe Inlet Geometry and Cone Angle on the Turbulent Boundary Layer and Heat Transfer in Conical Nozzles Operating with Air. Paper to be presented at the Ninth National ASME Heat Transfer Conference, Aug. 1967.

6. Wesoky, Howard L.: Boundary-Layer Measurements in Accelerated Flows Near Mach 1. NASA TN D-3882, 1967.

7. Bartz, D. R.: Turbulent Boundary-Layer Heat Transfer from Rapidly Accelerating Flow of Rocket Combustion Gases and of Heated Air. Advances in Heat Transfer, Vol. 2, James P. Hartnett and Thomas F. Irvine, Jr., eds., Academic Press, 1965, pp. 1-108.

8. Fortini, Anthony; and Ehlers, Robert C.: Comparison of Experimental to Predicted Heat Transfer in a Bell-Shaped Nozzle with Upstream Flow Disturbances. NASA TN D-1743, 1963.

9. Back, L. H.; Massier, P. F.; and Gier, H. L.: Comparisons of Experimental with Predicted Wall Static-Pressure Distributions in Conical Supersonic Nozzles. Tech. Rep. 32-654 (NASA CR-59577) Jet Propulsion Lab., California Inst. Tech., Oct. 1964.

10. Back, L. H.; Massier, P. F.; and Cuffel, R. F.: A More Detailed Investigation of Wall Static Pressure Distributions in a Conical Nozzle with a 45-Degree Half-Angle of Convergence and a 15-Degree Half-Angle of Divergence. Space Programs Summary No. 37-34, Vol. IV, Jet Propulsion Lab., California Inst. Tech., Aug. 31, 1965, pp. 143-149.

11. McBride, Bonnie, J.; Heimel, Sheldon; Ehlers, Janet G.; and Gordon, Sanford: Thermodynamic Properties to 6000° K for 210 Substances Involving the First 18 elements. NASA SP-3001, 1963.

12. Eckert, E. R. G.; and Drake, Robert M., Jr.: Heat and Mass Transfer. Second ed., McGraw-Hill Book Co., Inc., 1959.

13. Coles, D. E.: The Turbulent Boundary Layer in a Compressible Fluid. Rep. No. P-2417, The Rand Corp., Aug. 1961.

14. Nestler, D. E.; and Goetz, R.: Survey of Theoretical and Experimental Determinations of Skin Friction in Compressible Boundary Layers. Part II. The Turbulent Boundary Layer on a Flat Plate. Rep. No. R58SD270, General Electric Co., Jan. 29, 1959.

TABLE I. - INSTRUMENTATION FOR 30°-15° NOZZLES

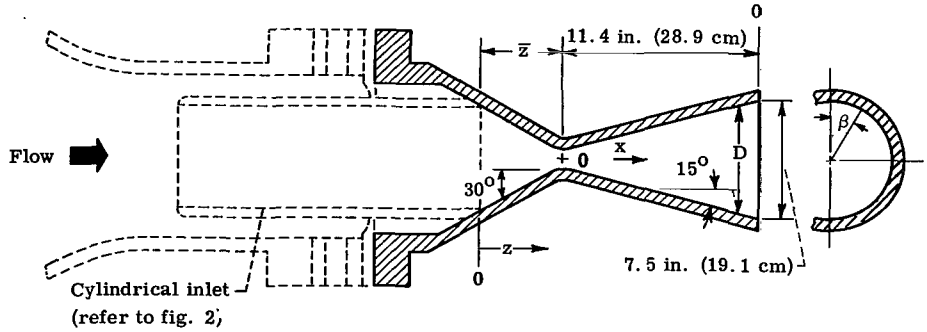

Inlet diameter		Axial distance, $\bar{z}$		Contraction area ratio, ϵ_c
in.	cm	in.	cm	
6.50	16.51	4.737	12.032	18.98
3.07	7.80	1.675	4.255	4.23
2.47	6.27	1.243	3.157	2.74

Station	Angular position, β, deg		Axial distance, x		Diameter, D	
	Pressure tap	Heat flux meter	in.	cm	in.	cm
2	231	51	-4.515	-11.468	6.250	15.875
3	129	309	-3.515	-8.928	5.092	12.934
4	180	0	-2.512	-6.380	3.934	9.992
5	231	51	-2.158	-5.481	3.528	8.961
6	283	103	-1.812	-4.602	3.128	7.945
7	334	154	-1.460	-3.708	2.722	6.914
8	26	206	-1.110	-2.819	2.316	5.883
9	77	257	-.613	-1.557	1.760	4.470
10	129	309	-.175	-.445	1.510	3.835
11	180	0	0	0	1.492	3.790
12	231	51	.130	.330	1.502	3.815
13	283	103	.255	.648	1.540	3.912
14	334	154	.392	.996	1.604	4.074
15	26	206	.634	1.610	1.732	4.399
16	77	257	1.221	3.101	2.042	5.187
17	180	0	2.736	6.949	2.858	7.259
18	180	↓	5.468	13.889	4.322	10.978
19	180	↓	8.201	20.831	5.792	14.712
20	180	↓	11.032	28.021	7.320	18.593

TABLE II. - INSTRUMENTATION FOR 60°-15° NOZZLE

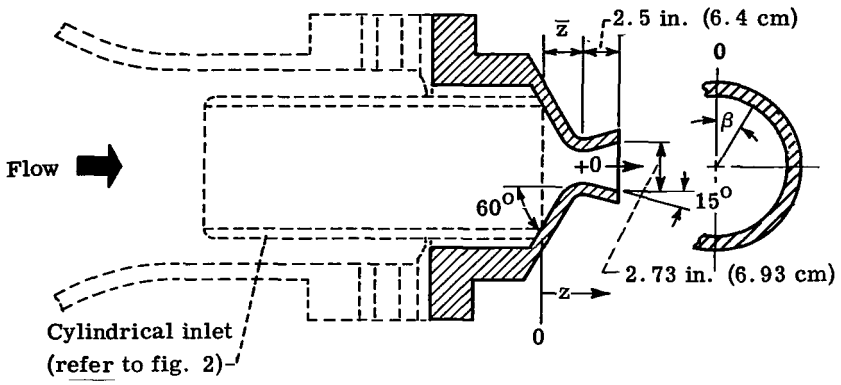

Inlet diameter		Axial distance, $\bar{z}$		Contraction area ratio, ϵ_c
in.	cm	in.	cm	
6.50	16.51	2.304	5.852	18.80
3.07	7.80	1.314	3.338	4.19

Station	Angular position, β, deg		Axial distance, x		Diameter, D	
	Pressure tap	Heat-flux meter	in.	cm	in.	cm
2	180	0	-2.085	-5.296	5.740	14.580
3	77	257	-1.752	-4.450	4.584	11.643
4	129	309	-1.635	-4.153	4.178	10.612
5	180	0	-1.515	-3.848	3.762	9.555
6	231	51	-1.206	-3.063	2.732	6.939
7	283	103	-1.020	-2.591	2.309	5.865
8	334	154	-.581	-1.476	1.736	4.409
9	26	206	-.146	-.371	1.516	3.851
10	77	257	0	0	1.499	3.807
11	129	309	.150	.381	1.521	3.863
12	180	0	.277	.704	1.565	3.975
13	231	51	.400	1.016	1.623	4.122
14	283	103	.622	1.580	1.741	4.422
15	334	154	1.209	3.071	2.053	5.215
16	26	206	2.140	5.436	2.545	6.464

TABLE III. - STATIC- TO TOTAL-PRESSURE RATIOS

(a) Nozzles

Station	30°-15° nozzle			60°-15° nozzle		
	Area ratio, A/A_t	Pressure ratio, P_s/P_0		Area ratio, A/A_t	Pressure ratio, P_s/P_0	
		Experiment	One-dimensional		Experiment	One-dimensional
2	17.548	0.99946	0.99921	14.663	0.99996	0.99891
3	11.648	.99847	.99827	9.352	.99907	.99731
4	6.952	.99565	.99509	7.769	.99826	.99610
5	5.591	.99325	.99241	6.299	.99691	.99405
6	4.395	.98887	.98768	3.322	.9811	.97825
7	3.328	.9804	.97830	2.373	.9560	.95631
8	2.410	.9624	.95768	1.341	.8227	.84342
9	1.392	.8399	.85703	1.023	.5680	.62815
10	1.024	.5733	.63117	1.000	.4681	.52828
11	1.000	.4600	.52828	1.030	.3383	.41399
12	1.013	.3733	.44998	1.090	.2612	.33605
13	1.065	.2785	.36165	1.172	.2222	.27469
14	1.156	.2084	.28457	1.349	.1765	.19898
15	1.348	.1820	.19938	1.876	.1103	.10530
16	1.873	.1125	.10556	2.883	.0545	.05050
17	3.669	.0375	.03417	-----	-----	------
18	8.391	.0094	.00951	-----	-----	------
19	15.070	.0038	.00397	-----	-----	------
20	24.071	.0024	.00200	-----	-----	------

(b) Uncooled pipe inlets

Inlet diameter		Nominal area ratio, A/A_t	Pressure ratio, P_s/P_0	
in.	cm		Experiment	One-dimensional
6.50	16.51	18.89	0.99932	0.9993
3.07	7.80	4.21	-------	.9866
[a]2.47	6.27	2.74	-------	.9683

[a]Denotes use with 30°-15° nozzle only.

TABLE IV. - EXPERIMENTAL

[Stagnation temperature

(a) 30°-

Station	Axial distance, x		Diameter, D		Inlet diameter, 6.50 in. (16.51 cm)					
	in.	cm	in.	cm	Axial distance, z		Stagnation pressure, P_0			
					in.	cm	299.5 psia	206.5 N/cm^2	160.2 psia	110.4 N/cm^2
							Heat-transfer coefficient based on enthalpy, h_i			
							lb/(in.^{2})(sec)	g/(cm^2)(sec)	lb/(in.^{2})(sec)	g/(cm^2)(sec)
2	-4.515	-11.468	6.250	15.875	0.222	0.564	9.5×10^{-4}	6.7×10^{-2}	5.9×10^{-4}	4.1×10^{-2}
3	-3.515	-8.928	5.092	12.934	1.222	3.104	10.8	7.6	5.8	4.1
4	-2.512	-6.380	3.934	9.992	2.225	5.652	17.1	12.0	7.8	5.5
5	-2.158	-5.481	3.528	8.961	2.579	6.551	19.7	13.9	9.7	6.8
6	-1.812	-4.602	3.128	7.945	2.925	7.430	22.4	15.7	12.1	8.5
7	-1.460	-3.708	2.722	6.914	3.277	8.324	25.2	17.7	14.7	10.3
8	-1.110	-2.819	2.316	5.883	3.627	9.213	32.3	22.7	19.4	13.6
9	-.613	-1.557	1.760	4.470	4.124	10.475	41.1	28.9	27.9	19.6
10	-.175	-.445	1.510	3.835	4.562	11.587	40.6	28.5	29.3	20.6
11	0	0	1.492	3.790	4.737	12.032	38.5	27.1	28.7	20.2
12	.130	.330	1.502	3.815	4.867	12.362	39.8	28.0	28.0	19.7
13	.255	.648	1.540	3.912	4.992	12.680	37.0	26.0	23.5	16.5
14	.392	.996	1.604	4.074	5.129	13.028	35.0	24.6	22.0	15.5
15	.634	1.610	1.732	4.399	5.371	13.642	31.2	21.9	19.4	13.6
16	1.221	3.101	2.042	5.187	5.958	15.133	24.8	17.4	15.5	10.9
17	2.736	6.949	2.858	7.259	7.473	18.981	16.8	11.8	8.5	6.0
18	5.468	13.889	4.322	10.978	10.205	25.921	5.2	3.6	3.0	2.1
19	8.201	20.831	5.792	14.712	12.938	32.863	2.7	1.9	1.5	1.1
20	11.032	28.021	7.320	18.593	15.769	40.053	2.1	1.5	1.6	1.1

(b) 60°-

Station	Axial distance, x		Diameter, D		Inlet diameter, 6.50 in. (16.51 cm)					
	in.	cm	in.	cm	Axial distance, z		Stagnation pressure, P_0			
					in.	cm	300.2 psia	207.0 N/cm^2	157.3 psia	108.4 N/cm^2
							Heat-transfer coefficient based on enthalpy, h_i			
							lb/(in.^{2})(sec)	g/(cm^2)(sec)	lb/(in.^{2})(sec)	g/(cm^2)(sec)
2	-2.085	-5.296	5.740	14.580	0.219	0.556	10.3×10^{-4}	7.2×10^{-2}	6.8×10^{-4}	4.8×10^{-2}
3	-1.752	-4.450	4.584	11.643	.552	1.402	11.1	7.8	7.1	5.0
4	-1.635	-4.153	4.178	10.612	.669	1.699	12.3	8.6	7.4	5.2
5	-1.515	-3.848	3.762	9.555	.789	2.004	14.0	9.8	8.2	5.8
6	-1.206	-3.063	2.732	6.939	1.098	2.789	25.8	18.1	10.4	7.3
7	-1.020	-2.591	2.309	5.865	1.284	3.261	36.6	25.7	11.9	8.4
8	-.581	-1.476	1.736	4.409	1.723	4.376	56.3	39.6	20.3	14.3
9	-.146	.371	1.516	3.851	2.158	5.481	60.6	42.6	27.1	19.1
10	0	0	1.499	3.807	2.304	5.852	59.6	41.9	27.3	19.2
11	.150	.381	1.521	3.863	2.454	6.233	57.3	40.3	31.8	22.4
12	.277	.704	1.565	3.975	2.581	6.556	53.1	37.3	29.3	20.6
13	.400	1.016	1.623	4.122	2.704	6.868	44.5	31.3	26.8	18.8
14	.622	1.580	1.741	4.422	2.926	7.432	39.0	27.4	23.0	16.2
15	1.209	3.071	2.053	5.215	3.513	8.923	30.0	21.1	17.5	12.3
16	2.140	5.436	2.545	6.464	4.444	11.288	19.8	13.9	11.7	8.2

HEAT-TRANSFER COEFFICIENTS

T_0, 970° R (~539° K).]

15° Nozzle

Inlet diameter, 3.07 in. (7.80 cm)						Inlet diameter, 2.47 in. (6.27 cm)					
Axial distance, z		Stagnation pressure, P_0				Axial distance, z		Stagnation pressure, P_0			
in.	cm	299.7 psia	206.6 N/cm^2	160.2 psia	110.4 N/cm^2	in.	cm	299.9 psia	206.8 N/cm^2	157.9 psia	108.9 N/cm^2
		Heat-transfer coefficient based on enthalpy, h_1						Heat-transfer coefficient based on enthalpy, h_1			
		lb/(in.^{2})(sec)	g/(cm^2)(sec)	lb/(in.^{2})(sec)	g/(cm^2)(sec)			lb/(in.^{2})(sec)	g/(cm^2)(sec)	lb/(in.^{2})(sec)	g/(cm^2)(sec)
-----	-----	----------	----------	----------	----------	------	------	----------	----------	----------	----------
-----	-----	----------	----------	----------	----------	------	------	----------	----------	----------	----------
-----	-----	----------	----------	----------	----------	------	------	----------	----------	----------	----------
-----	-----	----------	----------	----------	----------	------	------	----------	----------	----------	----------
-----	-----	----------	----------	----------	----------	------	------	----------	----------	----------	----------
0.215	0.546	36.2×10^{-4}	25.5×10^{-2}	21.3×10^{-4}	15.0×10^{-2}	------	------	----------	----------	----------	----------
.565	1.435	49.0	34.5	25.8	18.1	0.133	0.338	43.7×10^{-4}	30.7×10^{-2}	25.5×10^{-4}	17.9×10^{-2}
1.062	2.697	70.0	49.2	38.9	27.3	.630	1.600	71.4	50.2	43.8	30.8
1.500	3.810	70.8	49.8	44.6	31.4	1.068	2.713	86.5	60.8	50.5	35.5
1.675	4.255	65.7	46.2	38.5	27.1	1.243	3.157	72.3	50.8	44.8	31.5
1.805	4.585	69.5	48.9	41.1	28.9	1.373	3.487	67.6	47.5	43.7	30.7
1.930	4.902	57.2	40.2	35.2	24.7	1.498	3.805	64.0	45.0	38.0	26.7
2.067	5.250	50.1	35.2	35.6	25.0	1.635	4.153	53.8	37.8	34.5	24.3
2.309	5.865	45.2	31.8	27.1	19.1	1.877	4.768	48.7	34.2	28.4	20.0
2.896	7.356	33.8	23.8	20.0	14.1	2.464	6.259	35.1	24.7	20.5	14.4
4.411	11.204	17.2	12.1	10.1	7.1	3.979	10.107	17.2	12.1	10.0	7.0
7.143	18.143	5.8	4.1	3.3	2.3	6.711	17.046	5.7	4.0	3.3	2.3
9.876	25.085	3.0	2.1	1.8	1.3	9.444	23.988	2.9	2.0	1.7	1.2
12.707	28.313	2.4	1.7	1.7	1.2	12.275	31.179	2.1	1.5	1.8	1.3

15° Nozzle

Inlet diameter, 3.07 in. (7.80 cm)					
Axial distance, z		Stagnation pressure, P_0			
in.	cm	298.3 psia	205.6 N/cm^2	159.4 psia	109.9 N/cm^2
		Heat-transfer coefficient based on enthalpy, h_1			
		lb/(in.^{2})(sec)	g/(cm^2)(sec)	lb/(in.^{2})(sec)	g/(cm^2)(sec)
-----	-----	----------	----------	----------	----------
-----	-----	----------	----------	----------	----------
-----	-----	----------	----------	----------	----------
-----	-----	----------	----------	----------	----------
0.108	0.274	37.0×10^{-4}	26.0×10^{-2}	24.1×10^{-4}	16.9×10^{-2}
.294	.747	52.7	37.1	26.8	18.8
.733	1.862	88.1	61.9	42.4	29.8
1.168	2.967	84.9	59.7	49.2	34.6
1.314	3.338	80.4	56.5	47.9	33.7
1.464	3.719	74.1	52.1	42.6	30.0
1.591	4.041	66.4	46.7	39.2	27.6
1.714	4.354	58.5	41.1	31.2	21.9
1.936	4.917	46.9	33.0	28.5	20.0
2.523	6.408	35.6	25.0	20.8	14.6
3.454	8.773	21.2	14.9	12.2	8.6

TABLE V. - EXPERIMENTAL

[Stagnation temperature,

(a) 30°-

Station	Axial distance, x		Diameter, D		Inlet diameter, 6.50 in. (16.51 cm)					
	in.	cm	in.	cm	Axial distance, z		Stagnation pressure, P_0			
					in.	cm	299.5 psia	206.5 N/cm^2	157.8 psia	108.8 N/cm^2
							Wall temperature, T_w			
							°R	°K	°R	°K
2	-4.515	-11.468	6.250	15.875	0.222	0.564	702	390	654	363
3	-3.515	-8.928	5.092	12.934	1.222	3.104	712	396	651	362
4	-2.512	-6.380	3.934	9.992	2.225	5.652	763	424	682	379
5	-2.158	-5.481	3.528	8.961	2.579	6.551	780	433	705	392
6	-1.812	-4.602	3.128	7.945	2.925	7.430	793	441	726	403
7	-1.460	-3.708	2.722	6.914	3.277	8.324	806	448	747	415
8	-1.110	-2.819	2.316	5.883	3.627	9.213	824	458	771	428
9	-.613	-1.557	1.760	4.470	4.124	10.475	847	471	806	448
10	-.175	-.445	1.510	3.835	4.562	11.587	838	466	807	448
11	0	0	1.492	3.790	4.737	12.032	831	462	801	445
12	.130	.330	1.502	3.815	4.867	12.362	824	458	796	442
13	.255	.648	1.540	3.912	4.992	12.680	819	455	778	432
14	.392	.996	1.604	4.074	5.129	13.028	809	449	765	425
15	.634	1.610	1.732	4.399	5.371	13.642	799	444	754	419
16	1.221	3.101	2.042	5.187	5.958	15.133	776	431	731	406
17	2.736	6.949	2.858	7.259	7.473	18.981	726	403	667	371
18	5.468	13.889	4.322	10.978	10.205	25.921	621	345	589	327
19	8.201	20.831	5.792	14.712	12.938	32.863	578	321	557	309
20	11.032	28.021	7.320	18.593	15.769	40.053	569	316	560	311

(b) 60°-

Station	Axial distance, x		Diameter, D		Inlet diameter, 6.50 in. (16.51 cm)					
	in.	cm	in.	cm	Axial distance, z		Stagnation pressure, P_0			
					in.	cm	300.2 psia	207.0 N/cm^2	157.3 psia	108.4 N/cm^2
							Wall temperature, T_w			
							°R	°K	°R	°K
2	-2.085	-5.296	5.740	14.580	0.219	0.556	692	384	648	360
3	-1.752	-4.450	4.584	11.643	.552	1.402	698	388	647	361
4	-1.635	-4.153	4.178	10.612	.669	1.699	706	392	652	362
5	-1.515	-3.848	3.762	9.555	.789	2.004	724	402	665	369
6	-1.206	-3.063	2.732	6.939	1.098	2.789	793	441	691	384
7	-1.020	-2.591	2.309	5.865	1.284	3.261	829	461	709	394
8	-.581	-1.476	1.736	4.409	1.723	4.376	862	479	766	426
9	-.146	-.371	1.516	3.851	2.158	5.481	858	477	790	439
10	0	0	1.499	3.807	2.304	5.852	855	475	790	439
11	.150	.381	1.521	3.863	2.454	6.233	847	471	802	446
12	.277	.704	1.565	3.975	2.581	6.556	834	463	794	441
13	.400	1.016	1.623	4.122	2.704	6.868	823	457	775	431
14	.622	1.580	1.741	4.422	2.926	7.432	803	446	757	421
15	1.209	3.071	2.053	5.215	3.513	8.923	772	429	729	405
16	2.140	5.436	2.545	6.464	4.444	11.288	731	406	680	378

WALL TEMPERATURES

T_0, ~970° R (~539° K).]

15° Nozzle

Inlet diameter, 3.07 in. (7.80 cm)						Inlet diameter, 2.47 in. (6.27 cm)					
Axial distance, z		Stagnation pressure, P_0				Axial distance, z		Stagnation pressure, P_0			
in.	cm	299.7 psia	206.6 N/cm^2	160.2 psia	110.4 N/cm^2	in.	cm	299.9 psia	206.8 N/cm^2	157.9 psia	108.9 N/cm^2
		Wall temperature, T_w						Wall temperature, T_w			
		°R	°K	°R	°K			°R	°K	°R	°K
-------	------	---	---	---	---	------	------	---	---	---	---
-------	------	---	---	---	---	------	------	---	---	---	---
-------	------	---	---	---	---	------	------	---	---	---	---
-------	------	---	---	---	---	------	------	---	---	---	---
-------	------	---	---	---	---	------	------	---	---	---	---
0.215	0.546	833	463	780	433	------	------	---	---	---	---
.565	1.435	855	475	795	442	0.133	0.338	853	474	802	446
1.062	2.697	877	487	833	463	.630	1.600	885	492	846	470
1.500	3.810	872	484	837	465	1.068	2.713	887	493	852	473
1.675	4.255	861	478	823	457	1.243	3.157	873	485	839	466
1.805	4.585	862	479	822	457	1.373	3.487	867	482	833	463
1.930	4.902	845	469	806	448	1.498	3.805	858	477	819	455
2.067	5.250	832	462	795	442	1.635	4.153	843	468	806	448
2.309	5.865	822	457	779	433	1.877	4.768	833	463	789	438
2.896	7.356	795	442	748	416	2.464	6.259	805	447	762	423
4.411	11.204	723	402	672	373	3.979	10.107	732	407	682	379
7.143	18.143	620	344	582	323	6.711	17.046	633	352	597	332
9.876	25.085	575	319	551	306	9.444	23.988	588	327	566	314
12.707	28.313	563	313	553	307	12.275	31.179	577	321	569	316

15° Nozzle

Inlet diameter, 3.07 in. (7.80 cm)					
Axial distance, z		Stagnation pressure, P_0			
in.	cm	298.3 psia	205.6 N/cm^2	159.4 psia	109.9 N/cm^2
		Wall temperature, T_w			
		°R	°K	°R	°K
-----	-----	---	---	---	---
-----	-----	---	---	---	---
-----	-----	---	---	---	---
-----	-----	---	---	---	---
0.108	0.274	829	461	795	442
.294	.747	863	479	812	451
.733	1.862	893	496	848	471
1.168	2.967	882	490	851	473
1.314	3.338	876	487	847	471
1.464	3.719	865	481	834	463
1.591	4.041	851	473	819	455
1.714	4.354	840	467	809	449
1.936	4.917	820	456	787	437
2.523	6.408	791	439	751	417
3.454	8.773	740	411	707	393

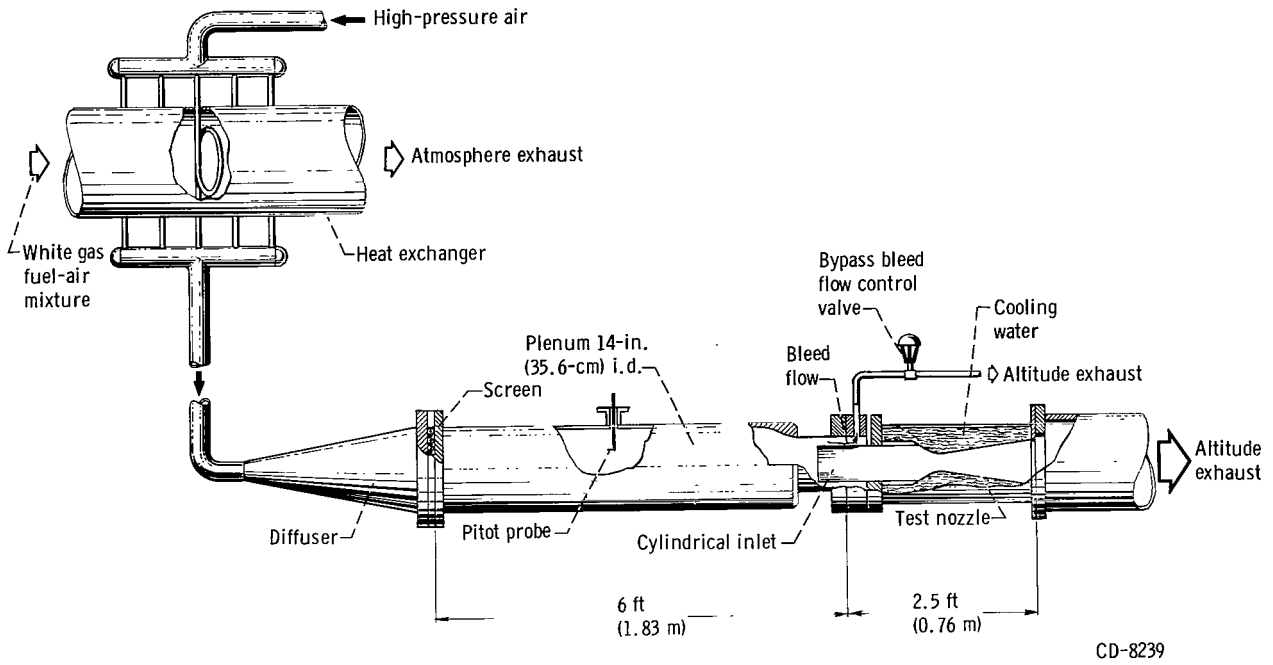

Figure 1. - Schematic diagram of nozzle heat-transfer facility.

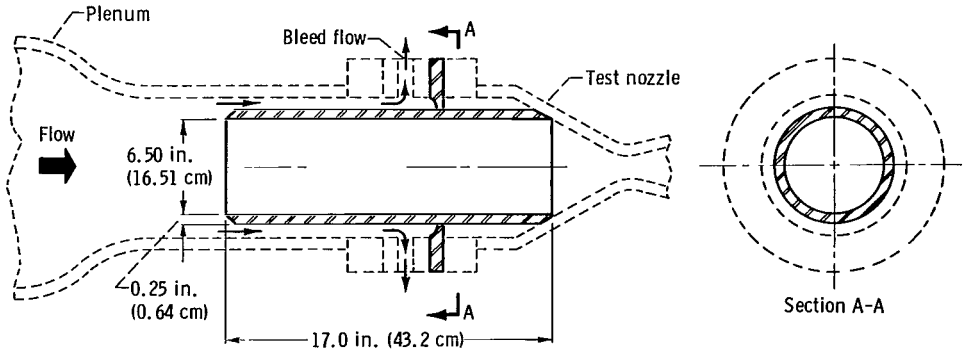

(a) 6.50-Inch (16.51-cm) inside diameter inlet used with 30° and 60° half-angle of convergence nozzles.

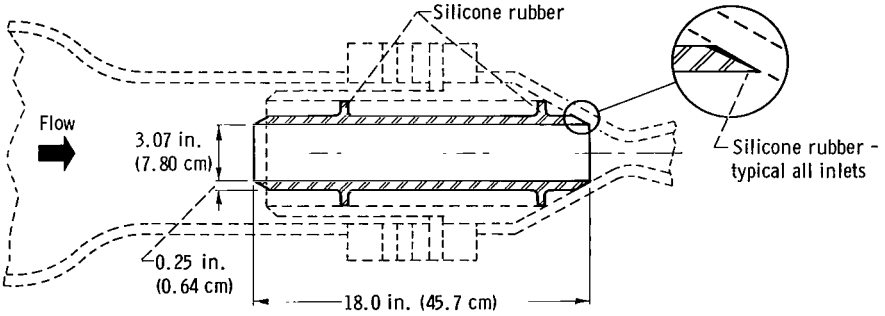

(b) 3.07-Inch (7.80-cm) inside diameter inlet used with 30° and 60° half-angle of convergence nozzles.

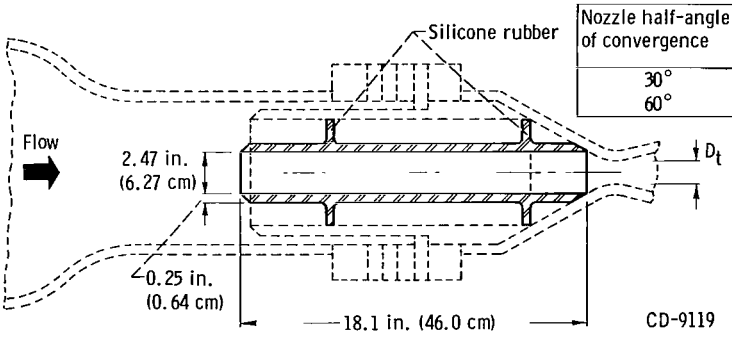

Nozzle half-angle of convergence	Local throat diameter, D_t	
	in.	cm
30°	1.492	3.790
60°	1.499	3.807

(c) 2.47-Inch (6.27-cm) inside diameter inlet used with 30° half-angle of convergence nozzle.

Figure 2. - Uncooled AISI 304 stainless-steel pipe inlets.

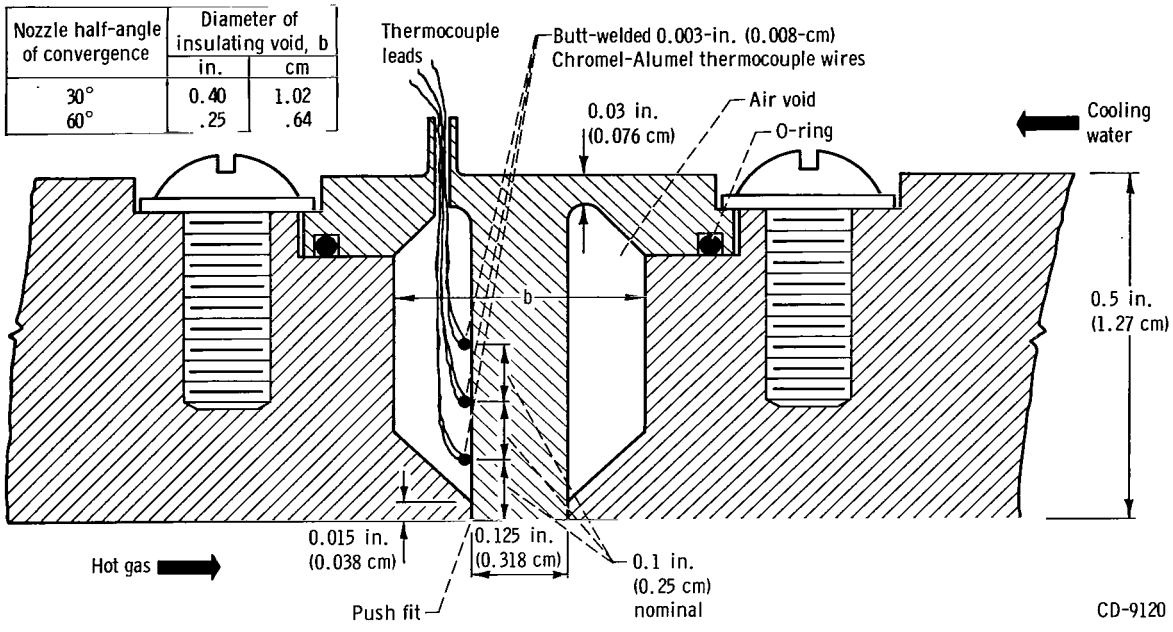

Figure 3. - Inconel heat-flux meter.

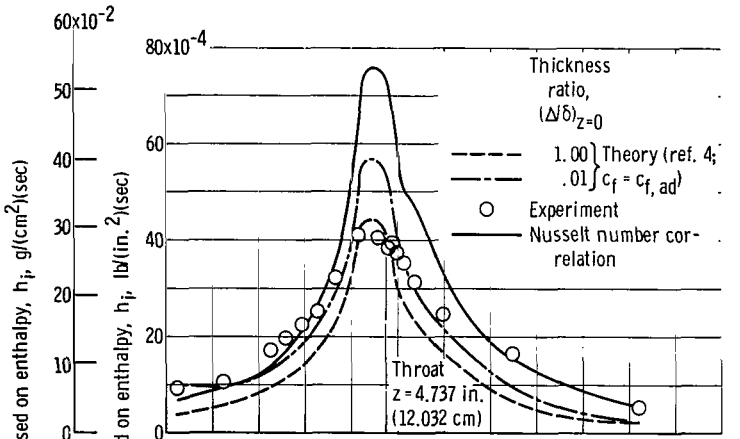

(a) Stagnation temperature T_0, 969.9° R (538.8° K); stagnation pressure P_0, 299.5 pounds per square inch (206.5 N/cm^2) absolute.

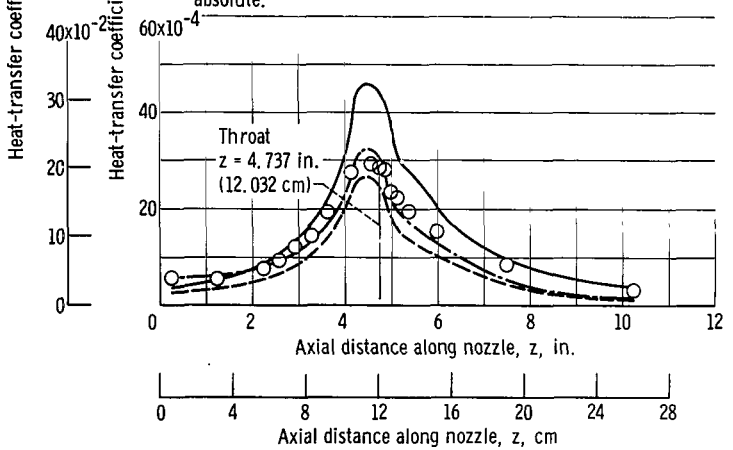

(b) Stagnation temperature T_0, 970.6° R (539.2° K); stagnation pressure P_0, 157.8 pounds per square inch (108.8 N/cm^2) absolute.

Figure 4. - Experimental and predicted heat-transfer distributions in 30°-15° nozzle with 6.50-inch (16.51-cm) inside diameter by 17.0-inch (43.2-cm) long uncooled pipe inlet.

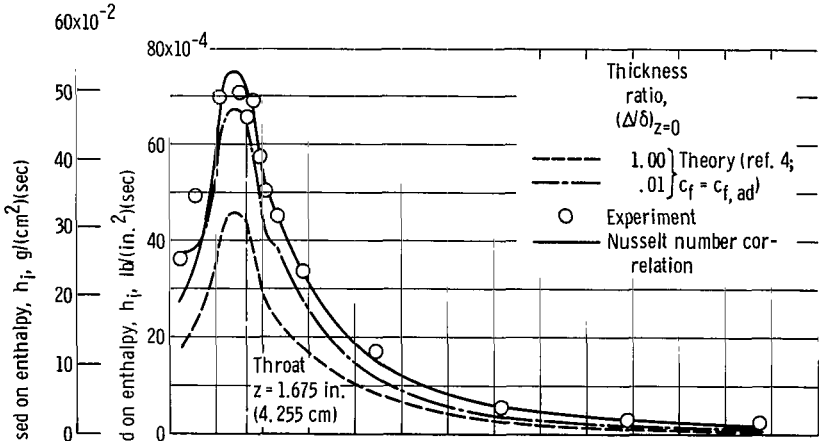

(a) Stagnation temperature T_0, 965.3° R (536.3° K); stagnation pressure P_0, 299.7 pounds per square inch (206.6 N/cm^2) absolute.

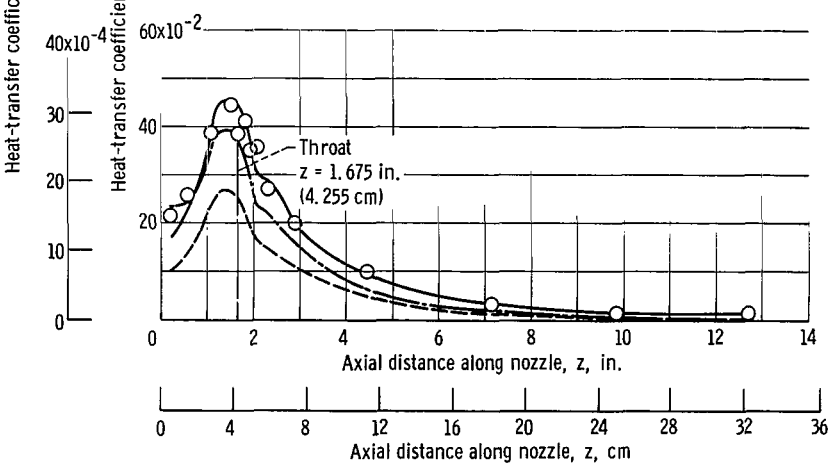

(b) Stagnation temperature T_0, 964.1° R (535.6° K); stagnation pressure P_0, 160.2 pounds per square inch (110.4 N/cm^2) absolute.

Figure 5. - Experimental and predicted heat-transfer distributions in 30°-15° nozzle with 3.07-inch (7.80-cm) inside diameter by 18.0-inch (45.7-cm) long uncooled pipe inlet.

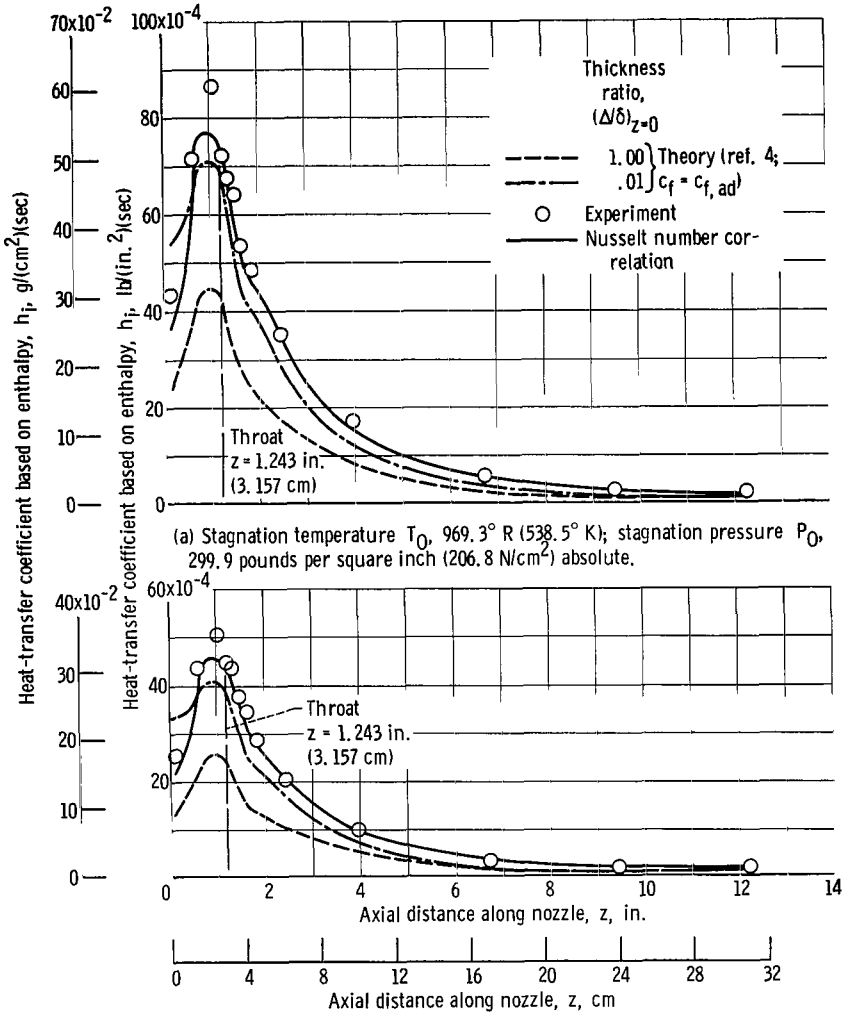

(a) Stagnation temperature T_0, 969.3° R (538.5° K); stagnation pressure P_0, 299.9 pounds per square inch (206.8 N/cm^2) absolute.

(b) Stagnation temperature T_0, 967.6° R (537.6° K); stagnation pressure P_0, 157.9 pounds per square inch (108.9 N/cm^2) absolute.

Figure 6. - Experimental and predicted heat-transfer distributions in 30°-15° nozzle with 2.47-inch (6.27-cm) inside diameter by 18.1-inch (46.0-cm) long uncooled pipe inlet.

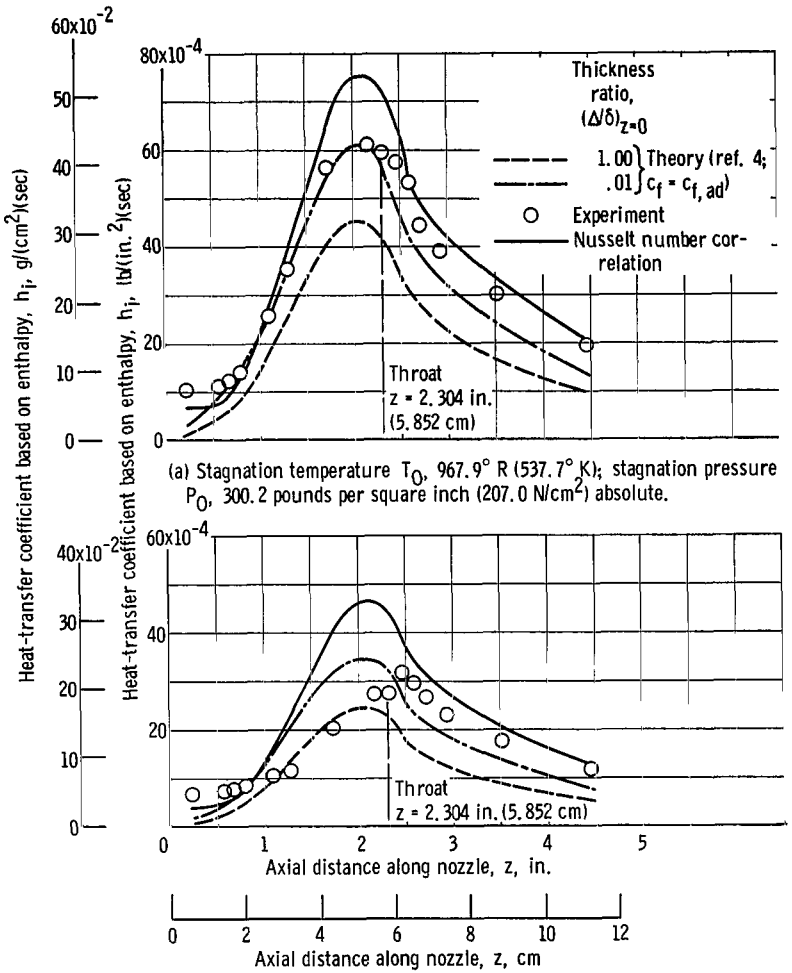

(a) Stagnation temperature T_0, 967.9° R (537.7° K); stagnation pressure P_0, 300.2 pounds per square inch (207.0 N/cm^2) absolute.

(b) Stagnation temperature T_0, 975.2° R (541.8° K); stagnation pressure P_0, 157.3 pounds per square inch (108.4 N/cm^2) absolute.

Figure 7. - Experimental and predicted heat-transfer distributions in 60°-15° nozzle with 6.50-inch (16.51-cm) inside diameter by 17.0-inch (43.2-cm) long uncooled pipe inlet.

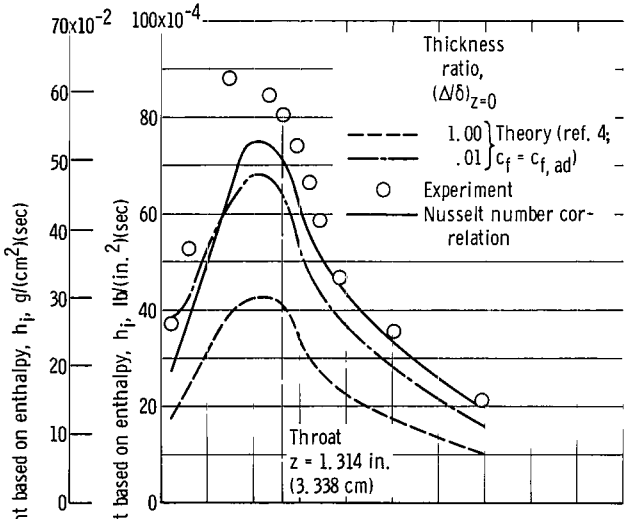

(a) Stagnation temperature T_0, 969.8° R (538.8° K); stagnation pressure P_0, 298.3 pounds per square inch (205.6 N/cm^2) absolute.

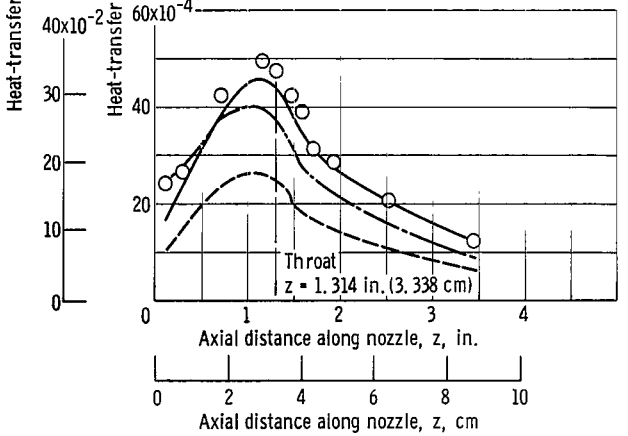

(b) Stagnation temperature T_0, 968.1° R (537.8° K); stagnation pressure P_0, 159.4 pounds per square inch (109.9 N/cm^2) absolute.

Figure 8. - Experimental and predicted heat-transfer distributions in 60°-15° nozzle with 3.07-inch (7.80-cm) inside diameter by 18.0-inch (45.7-cm) long uncooled pipe inlet.

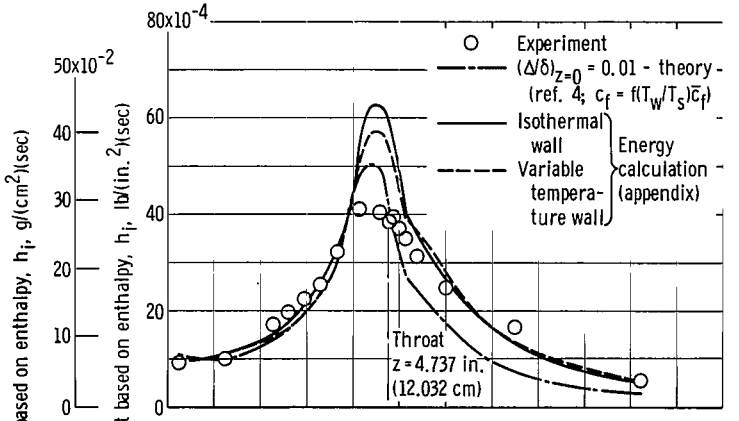

(a) Stagnation temperature T_0, 969.9° R (538.9° K); stagnation pressure P_0, 299.5 pounds per square inch (206.5 N/cm^2) absolute.

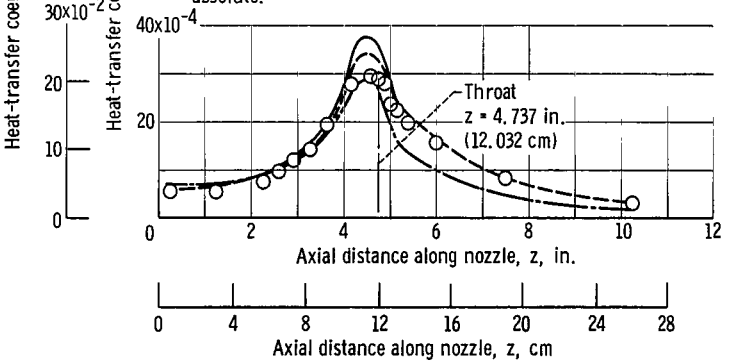

(b) Stagnation temperature T_0, 970.6° R (539.2° K); stagnation pressure P_0, 157.8 pounds per square inch (108.8 N/cm^2) absolute.

Figure 9. - Experimental and predicted heat-transfer distributions in 30°-15° nozzle with 6.50-inch (16.51-cm) inside diameter by 17.0-inch (43.2-cm) long uncooled pipe inlet.

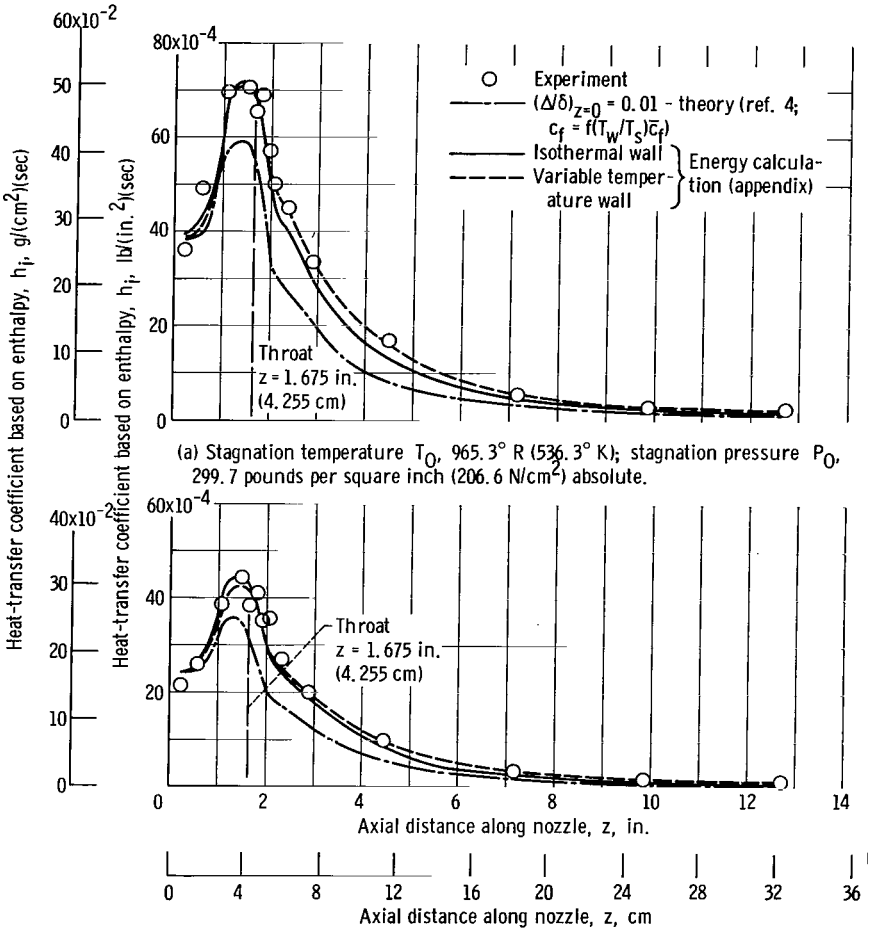

(a) Stagnation temperature T_0, 965.3° R (536.3° K); stagnation pressure P_0, 299.7 pounds per square inch (206.6 N/cm^2) absolute.

(b) Stagnation temperature T_0, 964.1° R (535.6° K); stagnation pressure P_0, 160.2 pounds per square inch (110.4 N/cm^2) absolute.

Figure 10. - Experimental and predicted heat-transfer distributions in 30°-15° nozzle with 3.07-inch (7.80-cm) inside diameter by 18.0-inch (45.7-cm) long uncooled pipe inlet.

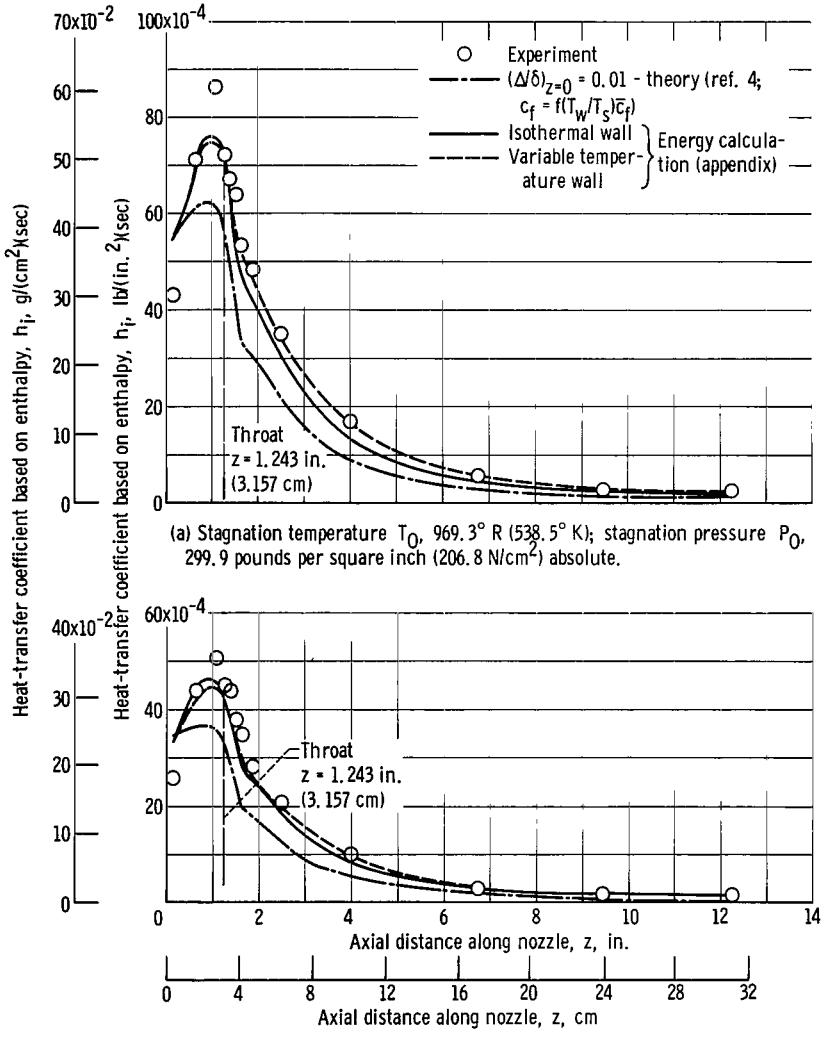

(a) Stagnation temperature T_0, 969.3° R (538.5° K); stagnation pressure P_0, 299.9 pounds per square inch (206.8 N/cm^2) absolute.

(b) Stagnation temperature T_0, 967.6° R (537.6° K); stagnation pressure P_0, 157.9 pounds per square inch (108.9 N/cm^2) absolute.

Figure 11. - Experimental and predicted heat-transfer distributions in 30°-15° nozzle with 2.47-inch (6.27-cm) inside diameter by 18.1-inch (46.0-cm) long uncooled pipe inlet.

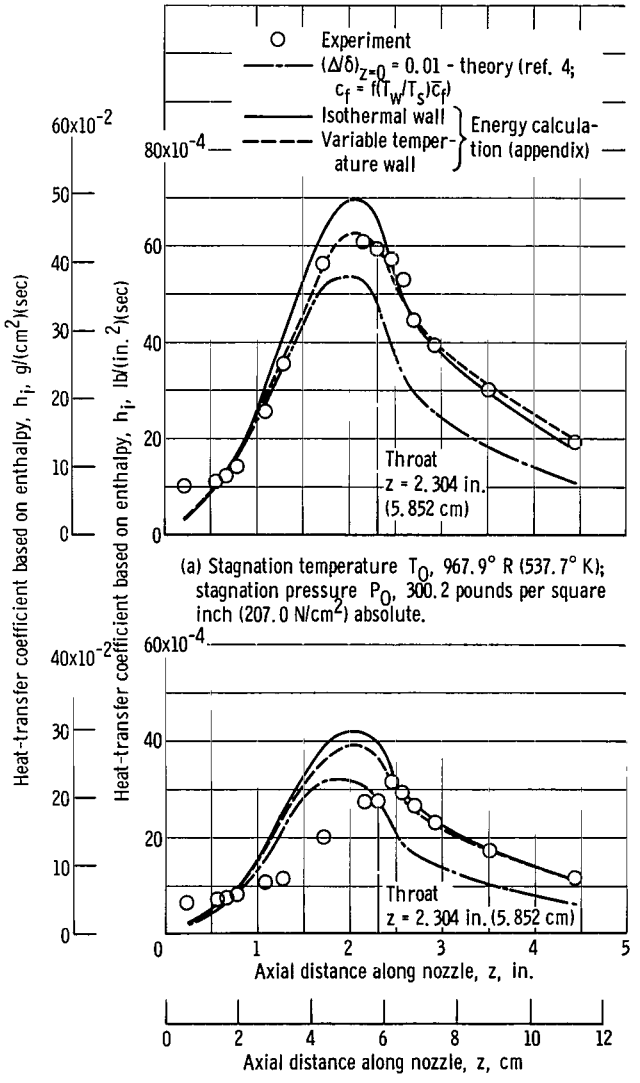

(a) Stagnation temperature T_0, 967.9° R (537.7° K); stagnation pressure P_0, 300.2 pounds per square inch (207.0 N/cm^2) absolute.

(b) Stagnation temperature T_0, 975.2° R (541.8° K); stagnation pressure P_0, 157.3 pounds per square inch (108.4 N/cm^2) absolute.

Figure 12. - Experimental and predicted heat-transfer distributions in 60°-15° nozzle with 6.50-inch (16.51-cm) inside diameter by 17.0-inch (43.2-cm) long uncooled pipe inlet.

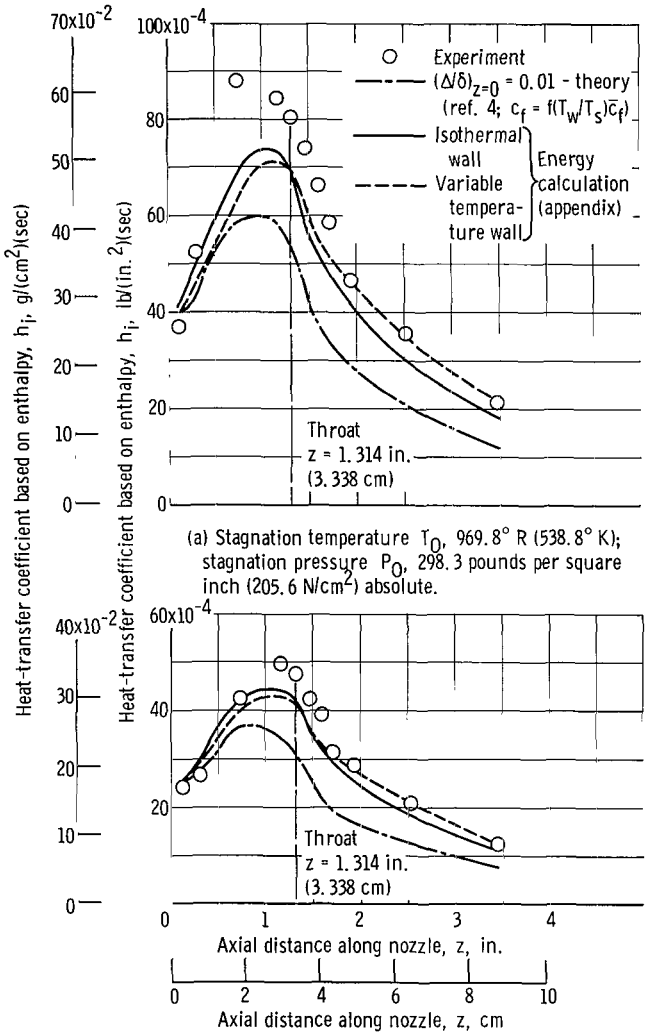

(a) Stagnation temperature T_0, 969.8° R (538.8° K); stagnation pressure P_0, 298.3 pounds per square inch (205.6 N/cm^2) absolute.

(b) Stagnation temperature T_0, 968.1° R (537.8° K); stagnation pressure P_0, 159.4 pounds per square inch (109.9 N/cm^2) absolute.

Figure 13. - Experimental and predicted heat-transfer distributions in 60°-15° nozzle with 3.07-inch (7.80-cm) inside diameter by 18.0-inch (45.7-cm) long uncooled pipe inlet.

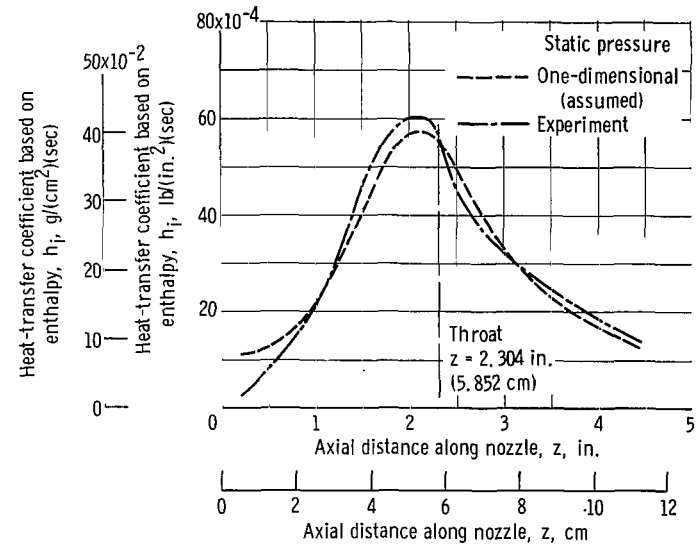

Figure 14. - Predicted heat-transfer distributions in 60°-15° nozzle with 6.50-inch (16.51-cm) inside diameter by 17.0-inch (43.2-cm) long uncooled pipe inlet using one-dimensional and measured static pressures. Stagnation temperature T_0, 967.9° R (537.7° K); stagnation pressure P_0, 300.2 pounds per square inch (207.0 N/cm^2) absolute. Theory (ref. 4; $c_f = c_{f,ad}$).

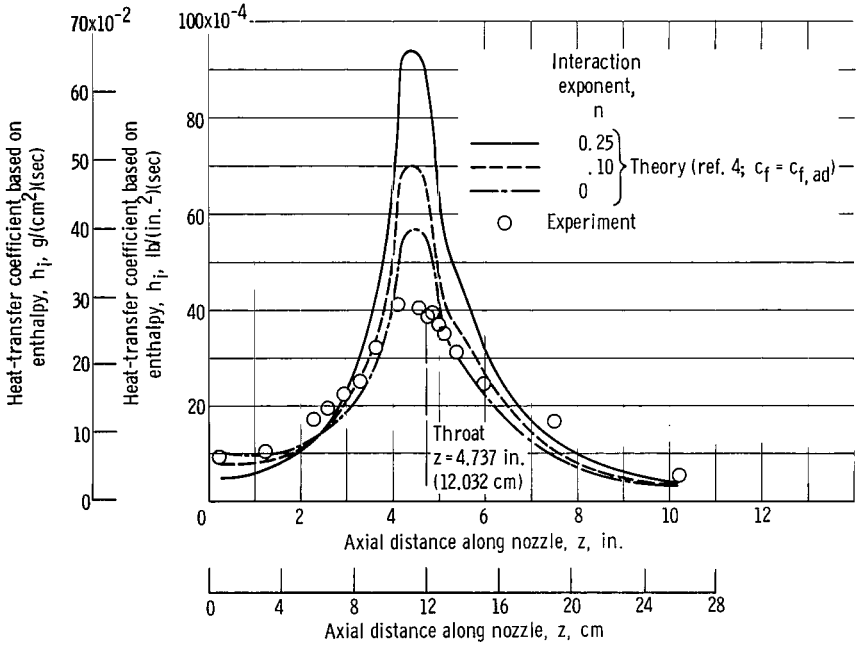

Figure 15. - Influence of interaction coefficient on predicted heat-transfer coefficients for 30°-15° nozzle operating with 6.50-inch (16.51-cm) inside diameter by 17.0-inch (43.2-cm) long uncooled pipe inlet. Stagnation temperature T_0, 969.9° R (538.8° K); stagnation pressure P_0, 299.5 pounds per square inch (206.5 N/cm^2) absolute.

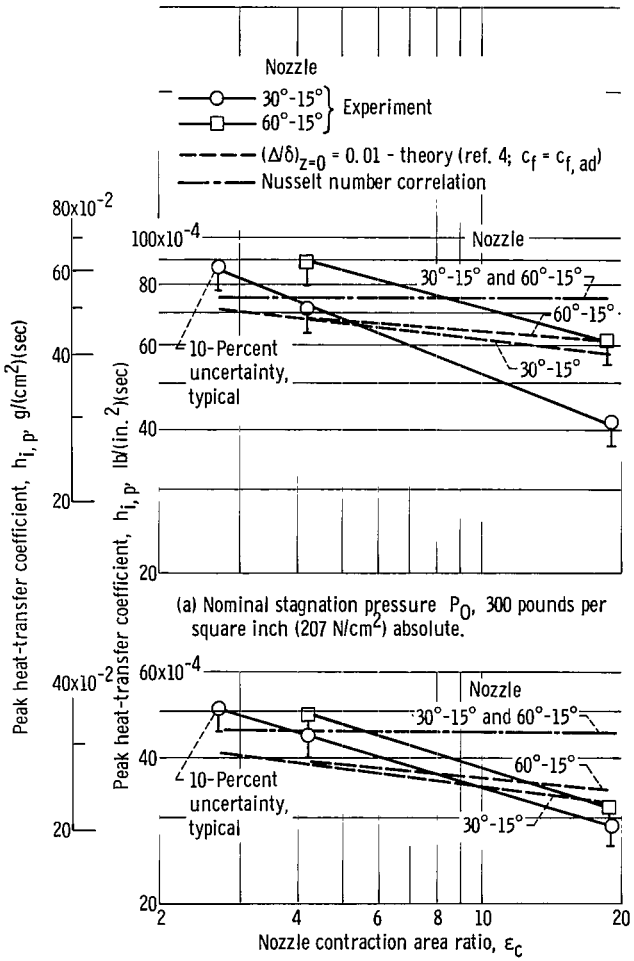

(a) Nominal stagnation pressure P_0, 300 pounds per square inch (207 N/cm^2) absolute.

(b) Nominal stagnation pressure P_0, 160 pounds per square inch (110 N/cm^2) absolute.

Figure 16. - Variation of peak heat-transfer coefficient with contraction area ratio. Stagnation temperature T_0, ~970° R (~539° K).

"The aeronautical and space activities of the United States shall be conducted so as to contribute . . . to the expansion of human knowledge of phenomena in the atmosphere and space. The Administration shall provide for the widest practicable and appropriate dissemination of information concerning its activities and the results thereof."

—NATIONAL AERONAUTICS AND SPACE ACT OF 1958

NASA SCIENTIFIC AND TECHNICAL PUBLICATIONS

TECHNICAL REPORTS: Scientific and technical information considered important, complete, and a lasting contribution to existing knowledge.

TECHNICAL NOTES: Information less broad in scope but nevertheless of importance as a contribution to existing knowledge.

TECHNICAL MEMORANDUMS: Information receiving limited distribution because of preliminary data, security classification, or other reasons.

CONTRACTOR REPORTS: Scientific and technical information generated under a NASA contract or grant and considered an important contribution to existing knowledge.

TECHNICAL TRANSLATIONS: Information published in a foreign language considered to merit NASA distribution in English.

SPECIAL PUBLICATIONS: Information derived from or of value to NASA activities. Publications include conference proceedings, monographs, data compilations, handbooks, sourcebooks, and special bibliographies.

TECHNOLOGY UTILIZATION PUBLICATIONS: Information on technology used by NASA that may be of particular interest in commercial and other non-aerospace applications. Publications include Tech Briefs, Technology Utilization Reports and Notes, and Technology Surveys.

Details on the availability of these publications may be obtained from:

SCIENTIFIC AND TECHNICAL INFORMATION DIVISION

NATIONAL AERONAUTICS AND SPACE ADMINISTRATION

Washington, D.C. 20546